



LAWRENCE
LIVERMORE
NATIONAL
LABORATORY

Performance of a Nanometer Resolution Beam Position Monitor System

Vladimir Vogel, Mark Slater, David Ward, Hitoshi Hayano, Yosuke Honda, Nobuhiro Terunuma, Junji Urakawa, Yury Kolomensky, Toyoko Orimoto, Carl Chung, Pete Fitsos, Jeff Gronberg, Sean Walston, Glen White, Joe Frisch, Justin May, Douglas McCormick, Marc Ross, Steve Smith, Tonee Smith, Stewart Boogert, Alexey Lyapin, Stephen Malton, David Miller

October 18, 2005

Nanobeam 2005
Kyoto, Japan
October 17, 2005 through October 21, 2005

Disclaimer

This document was prepared as an account of work sponsored by an agency of the United States Government. Neither the United States Government nor the University of California nor any of their employees, makes any warranty, express or implied, or assumes any legal liability or responsibility for the accuracy, completeness, or usefulness of any information, apparatus, product, or process disclosed, or represents that its use would not infringe privately owned rights. Reference herein to any specific commercial product, process, or service by trade name, trademark, manufacturer, or otherwise, does not necessarily constitute or imply its endorsement, recommendation, or favoring by the United States Government or the University of California. The views and opinions of authors expressed herein do not necessarily state or reflect those of the United States Government or the University of California, and shall not be used for advertising or product endorsement purposes.

Performance of a Nanometer Resolution BPM System

Vladimir Vogel
DESY, Hamburg, Germany

Hitoshi Hayano, Yosuke Honda, Nobuhiro Terunuma, Junji Urakawa
KEK, Tsukuba-shi, Ibaraki-ken, Japan

Yury Kolomensky, Toyoko Orimoto
Lawrence Berkeley National Laboratory, Berkeley, California, USA

Carl Chung, Pete Fitsos, Jeff Gronberg, Sean Walston
Lawrence Livermore National Laboratory, Livermore, California, USA

Glen White
Queen Mary College, London, UK and Stanford Linear Accelerator Center, Menlo Park, California, USA

Joe Frisch, Justin May, Douglas McCormick, Marc Ross, Steve Smith, Tonee Smith
Stanford Linear Accelerator Center, Menlo Park, California, USA

Mark Slater, David Ward
University of Cambridge, Cambridge, UK

Stewart Boogert, Alexey Lyapin, Stephen Malton, David Miller
University College, London, UK
(Dated: November 2, 2005)

International Linear Collider (ILC) interaction region beam sizes and component position stability requirements will be as small as a few nanometers. It is important to the ongoing ILC design effort to demonstrate that these tolerances can be achieved – ideally using beam-based stability measurements. It has been estimated that an RF cavity BPM with modern waveform processing could provide a position measurement resolution of less than one nanometer. Such a system could form the basis of the desired beam-based stability measurement, as well as be used for other specialized purposes. We have developed a high resolution RF cavity BPM and associated electronics. A triplet comprised of these BPMs has been installed in the extraction line of the KEK Accelerator Test Facility (ATF) for testing with its ultra-low emittance beam. The three BPMs are rigidly mounted inside an alignment frame on six variable-length struts which can be used to move the BPMs in position and angle. We have developed novel methods for extracting the position and tilt information from the BPM signals including a robust calibration algorithm which is immune to beam jitter. To date, we have been able to demonstrate a resolution of approximately 20 nm over a dynamic range of $\pm 20 \mu\text{m}$. We report on the progress of these ongoing tests.

I. INTRODUCTION

The design for the International Linear Collider (ILC) calls for beams which are focused down to a few nanometers at the interaction point. This poses unique engineering challenges which must be overcome. To wit, final focus components must be effectively stabilized at the nanometer level.

Some years ago, LINX was proposed as a new facility at SLAC to support engineering studies of, among other things, stabilization techniques for beamline components [1]. One goal was to demonstrate nanometer stability of colliding beams. Located in the SLD collider hall, LINX was to reuse much of the existing hardware of the SLC and SLD. During the Nanobeam 2002 Workshop in Lausanne, Switzerland in September of that year, it was suggested that nanometer resolution beam position monitors

(BPMs) could verify the nanometer level vibration stability without the LINX beam-beam collision project. The intent of our experiment is to understand the limits of BPM performance and to evaluate their role in overcoming some of the thorny engineering issues the interaction region of the ILC presents.

The intrinsic resolution of a BPM is limited by the signal to noise ratio of the system: The signal voltage of the BPM is determined by the beam's energy loss to the antisymmetric transverse magnetic TM_{110} mode (discussed in some detail in section II) and by the external coupling of the waveguide; the overall noise of the system comes from thermal noise as well as contamination from the symmetric transverse magnetic TM_{010} mode (again, see section II). It has been estimated that an RF cavity BPM along with state-of-the-art waveform processing could have a resolution below one nanometer [4].

With sufficient resolution, other beam-diagnostic measurements are also feasible. For example, a finite-length bunch having either a non-zero angle of obliquity or angle of attack (relative to the orientation of the cavity) produces a signal – hereafter referred to simply as “tilt” – which is in quadrature to the position signal produced by a simple displacement of a very short bunch. It is therefore possible to independently measure both the position and tilt of the beam by using in-phase/quadrature-phase (I/Q) demodulation of the signal from the cavity BPM: The conversion from I and Q to position and tilt is a simple rotation.

This paper describes the NanoBPM experiment and discusses recent progress in the collaboration’s efforts to develop nanometer resolution cavity BPMs.

II. THEORY OF CAVITY BPMS

When a bunch transits a cavity, the field of the bunch excites the eigenmodes of the electromagnetic fields within the cavity. For the case of a cavity in the shape of a right circular cylinder (ignoring the effects of the beam pipe openings), the frequencies of the eigenmodes naturally depend on the length L and radius R of the cavity. For cavities with $L < 2.03R$, which is the case here, the first transverse magnetic (TM) mode is the fundamental oscillation of the cavity [5].

For beams near the center of the cavity, the TM_{010} or monopole mode has the highest excitation of all the modes, is symmetric, and is proportional to the charge of the bunch. The explicit expressions for the fields of the TM_{010} mode are

$$E_z = CJ_0 \left(\frac{j_{01}r}{R} \right) e^{i\omega_{010}t} \quad (1)$$

$$H_r = 0 \quad (2)$$

$$H_\phi = -iC \frac{\omega_{010}\epsilon_0 R}{j_{01}} J_0' \left(\frac{j_{01}r}{R} \right) e^{i\omega_{010}t}. \quad (3)$$

where C is proportional to the amplitude of the oscillation, J_m is a Bessel function of the first kind of order m , and j_{mn} is the n th root of the equation $J_m(j) = 0$; $j_{01} = 2.405$ [6]. These fields are illustrated in Figure 1.

The TM_{110} or dipole mode, however, is antisymmetric and its amplitude has a strong dependence on the transverse offset of the beam relative to the electrical center of the cavity; the power thus has a quadratic dependence on the offset. The phase depends on the direction of the offset. The explicit expressions for the fields of the TM_{110} mode are

$$E_z = CJ_1 \left(\frac{j_{11}r}{R} \right) \cos(\phi) e^{i\omega_{110}t} \quad (4)$$

$$H_r = -iC \frac{\omega_{110}\epsilon_0 R^2}{j_{11}^2 r} J_1 \left(\frac{j_{11}r}{R} \right) \sin(\phi) e^{i\omega_{110}t} \quad (5)$$

$$H_\phi = -iC \frac{\omega_{110}\epsilon_0 R}{j_{11}} J_1' \left(\frac{j_{11}r}{R} \right) \cos(\phi) e^{i\omega_{110}t} \quad (6)$$

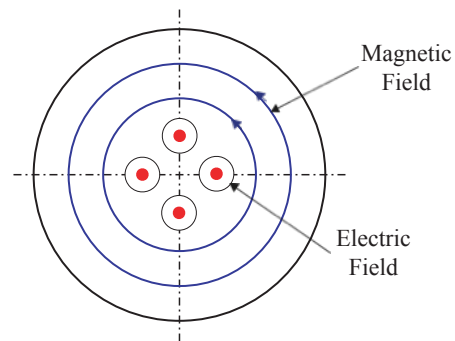


FIG. 1: The fields of the TM_{010} or monopole mode. The amplitude of the monopole mode is proportional to the bunch charge.

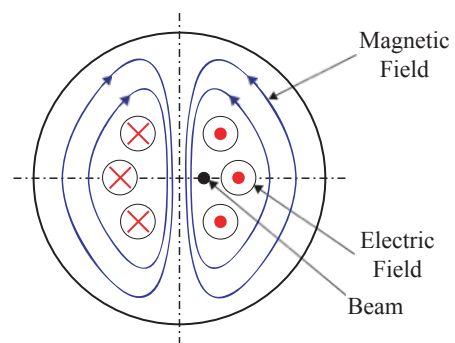


FIG. 2: The fields of the TM_{110} or dipole mode. The amplitude of the dipole mode has a strong dependence on offset of the beam relative to the electrical center of the cavity.

where $j_{11} = 3.832$ [6]. These fields are illustrated in Figure 2.

Physical cavities have finite values for the quality factor Q : They dissipate energy in the cavity walls as well as in any dielectric in the cavity. Each of the cavity’s resonant frequencies is therefore not simply a single frequency but rather is smeared out, and appreciable excitations can occur over a narrow band of frequencies around the eigenfrequency. The monopole mode can therefore have a finite tail at the dipole mode frequency, as illustrated in Figure 3. These components cannot be simply filtered out.

III. EXPERIMENTAL SETUP

This experiment employed three identical cavity BPMs designed at Budker Institute of Nuclear Physics (BINP) [7]. The resonant frequency of the dipole TM_{110} mode was 6426 MHz. The dipole mode – whose amplitude is comparatively small when the beam passes near the electrical center of the cavity – was selectively coupled out by two orthogonal slots – one each for x and y –

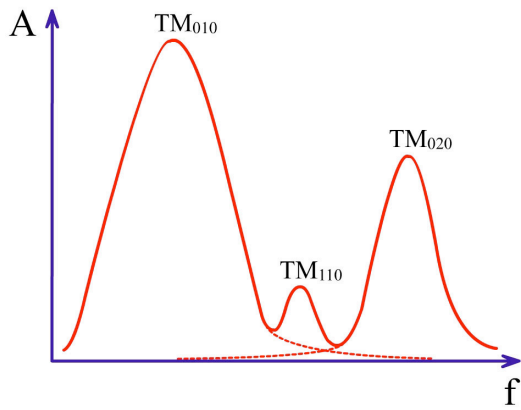


FIG. 3: The the first two monopole modes surround the (usually) much smaller amplitude dipole mode, and because of the finite Q of the cavity, have components at the dipole mode frequency.

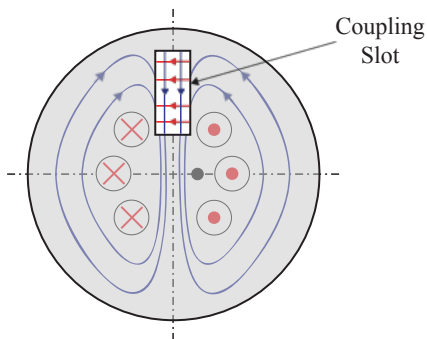


FIG. 4: The dipole mode was selectively coupled out by means of two long, narrow, radial slots on one face of the cavity. The electric field vector points circumferentially across the slot while the magnetic field vector points radially. (The slot shown is not to scale and is for illustrative purposes.) The cavities had two orthogonal slots corresponding to x and y .

which exploited the difference in the field structure of the monopole and dipole modes to reject the monopole mode – and in particular the side bands which reside at or near the dipole mode frequency. This is illustrated in Figure 4. A quarter view of the material boundaries of the BINP BPM cavities is shown in Figure 5.

To the three directional cavities must be added a fourth “reference” cavity whose monopole TM_{010} mode had a resonant frequency of 6426 MHz. The signal from this cavity was used to normalize the amplitudes of the signals from the three directional cavities to remove the effects of variations in the bunch charge; it also provided a single reference for comparing the phases of the signals from the three directional cavities. The signal from the reference cavity was also split with one part being passed through a crystal detector; this information was used to determine the time the bunch transited the apparatus.

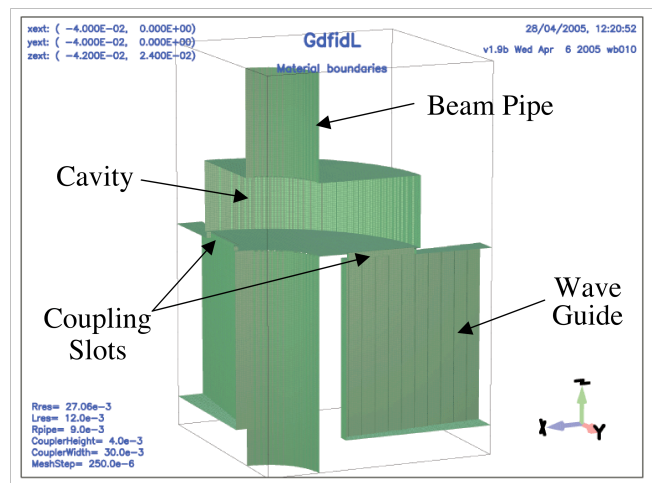


FIG. 5: A quarter view of the inside surface of a BINP BPM.

The three directional BPMs were located in the ATF extraction line and were rigidly mounted inside an alignment frame consisting of a steel space frame which was designed and built at LLNL. The entire alignment frame assembly was suspended by four variable length motorized legs and a non-motorized variable length center strut which allowed the alignment frame to be moved in x , y , yaw, pitch, and roll. Pure y , and yaw motion were possible; x motion included a small amount of roll while pitch necessarily changed the z position slightly. The physical layout of the experiment is illustrated in Figure 6. The Livermore space frame, before the BPMs were mounted inside, is shown in Figure 7. The reference cavity was not contained in the alignment frame, but was located a few centimeters downstream from the third directional BPM.

Each individual BPM was rigidly mounted on six variable length struts which allowed it to be moved by small amounts in x , y , z , yaw, pitch, and roll. The mounting scheme for a single BPM is illustrated in Figure 8. The structure of the hexapod struts is inherently stiff, and coupled with the rigidity of the Livermore space frame allowed rigid-body motion of the three BPMs. A strut is pictured in Figure 9.

Single bunch extractions from the ATF ring were used for all of our tests. Each ATF extraction contained between 6 and $7 \times 10^9 e^-$ at an energy of 1.28 GeV. The machine repetition rate was ~ 1 Hz.

The electronics used to process the raw signals from the BPMs may be summarized as follows:

1. Bandpass filter, 6426 MHz with 225 MHz bandwidth: Removed of out-of-band signals, most notably monopole mode which due to imperfect coupling slots may not be completely rejected
2. Amplifier, 20 dB gain
3. Mixer, 5950 MHz LO: Mix down to 476 MHz

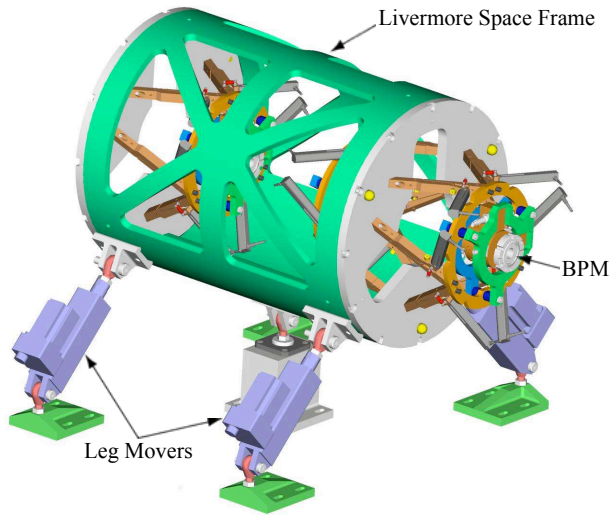


FIG. 6: The Livermore space frame served as the mounting platform for the three BINP BPMs.

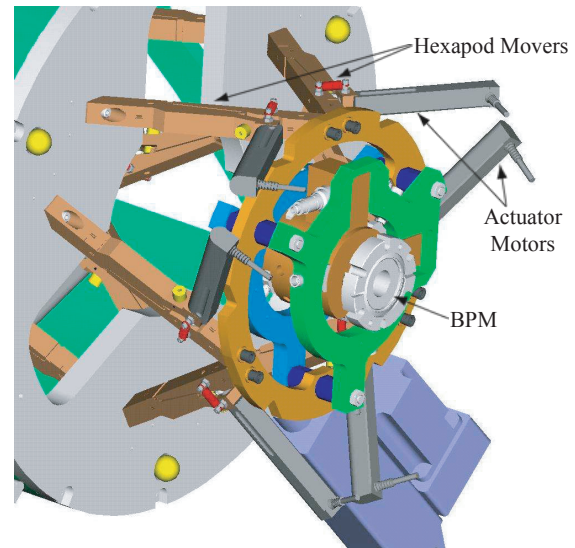


FIG. 8: The BPMs are mounted on hexapod strut movers.

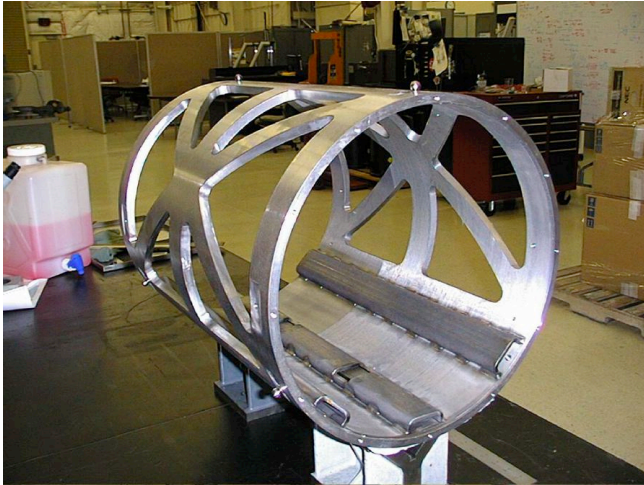


FIG. 7: The Livermore space frame held the entire three-BPM assembly rigid. The first vibrational mode was at 200 Hz.

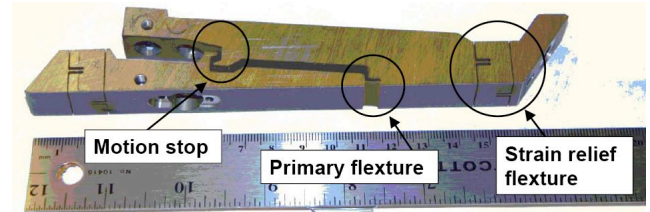


FIG. 9: Each hexapod strut employs a flexure with approximately a 12 to 1 mechanical advantage, i.e. a change in the gap results in a 1/12 change in length of the strut.

4. Lowpass filter, 700 MHz cutoff: Removed residual LO signal
5. Amplifier, 20 dB gain
6. Bandpass filter, 476 MHz with 20 MHz bandwidth: Removed out-of-band noise which could be aliased into the signal band
7. Mixer, 456 MHz LO: Mix down to 26 MHz
8. Lowpass filter, 30 MHz cutoff: Removed residual LO signal
9. Amplifier, 16 dB

10. Lowpass filter, 30 MHz cutoff: Removed out-of-band noise which could be aliased into the signal band

11. Digitizer, 14 bit, 100 Megasamples per second

This is diagrammed in Figure 10.

IV. WAVEFORM PROCESSING

In order to tease out the skin of beam position and trajectory from the raw BPM signals, precise determinations of the amplitudes and phases of the digitized waveforms were needed. A representative raw waveform is illustrated in Figure 11.

The process began by determining the decay rate Γ_i and the frequency ω_i for each of the six channels i as well as for the reference cavity signal. Each of the seven digitized waveforms were initially fitted with the equation

$$V = V_0 + Ae^{-\Gamma(t-t_0)} \sin[\omega(t-t_0) + \varphi], \quad (7)$$

where the values of A , Γ , ω , and φ were all considered as parameters to be determined by the fit. The pedestal

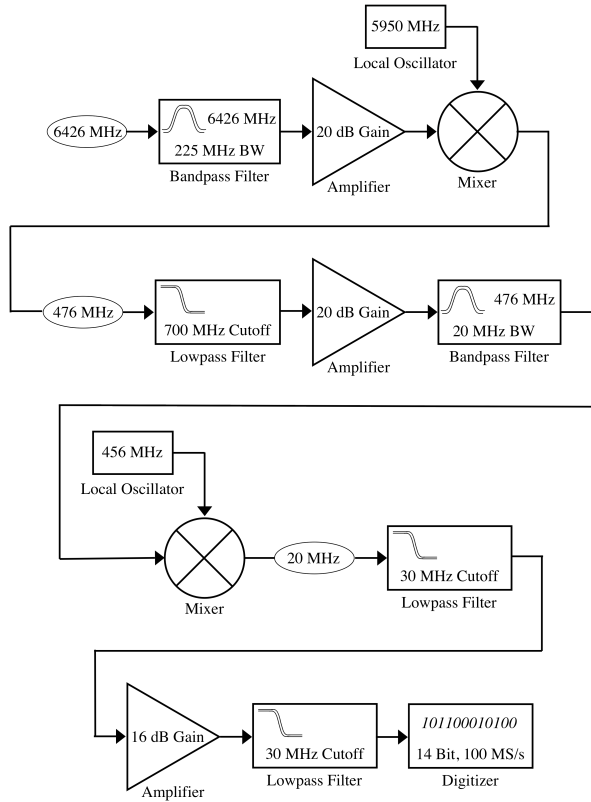


FIG. 10: The electronics used to process the signals from each channel.

value for the ADC, V_0 , was taken as the mean value for the first 20 or so samples in the waveform which occurred before the bunch transited the cavity. The value for t_0 was determined by fitting the midpoint of the rise of the signal from the crystal detector, as shown in Figure 12. All waveforms were fitted using only samples taken after the waveform was no longer saturated, or after 60 μs , whichever was later, with the latter criterion being employed to allow any monopole mode which had leaked through to decay away.

The decay rates Γ and the frequencies ω should not vary from event to event as these quantities are properties of the cavities themselves (a rather small variation on long time scales might be expected due to temperature variations of the cavities). For the six directional BPM channels, the Γ_i and ω_i were determined by taking the median value of the distribution of events with large amplitudes, typically defined as those events where the BPM has been moved a relatively large amount in such a way as to produce a large signal in channel i . For the special case of the reference cavity, the decay rate Γ_{Ref} and the frequency ω_{Ref} were determined by simply taking the median over all events.

Once all the decay rates Γ and frequencies ω had been determined, one of two methods were employed for the final determination of the amplitudes A and phases φ :

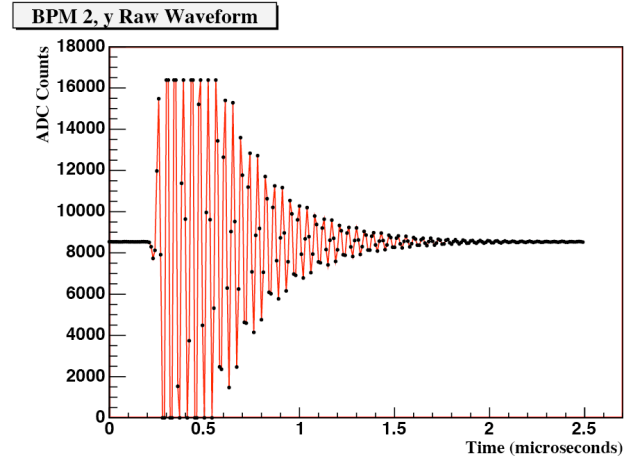


FIG. 11: An example of a raw waveform – this one happens to be from BPM 2, y . Note that in this case the samples between 0.3 μs and 0.6 μs are saturated.

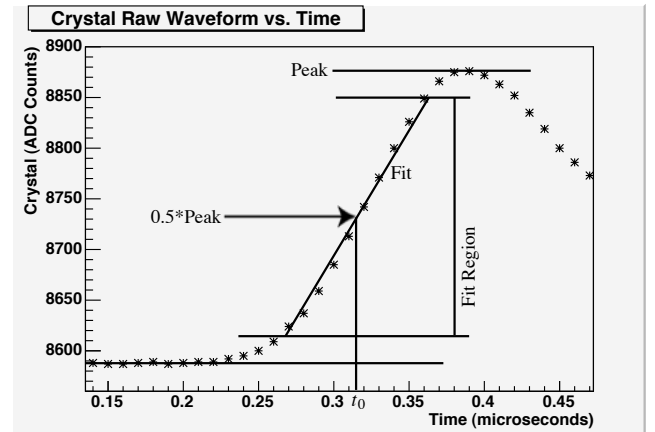


FIG. 12: The value for t_0 was determined on an event by event basis by fitting the rise of the signal from the crystal detector, and defining t_0 to be at the midpoint of the rise, i.e. the time corresponding to when the signal is 0.5 times the value at the peak. So that only the linear portion of the waveform is used, the top and bottom of the rise are excluded from the fit.

Fitting, or digital down-conversion. Each method will be discussed in some detail below.

The quantities I_i and Q_i were then calculated by normalizing each amplitude A_i and phase φ_i to the the reference cavity amplitude A_{Ref} and phase φ_{Ref} ,

$$I_i = \frac{A_i}{A_{\text{Ref}}} \cos(\varphi_i - \varphi_{\text{Ref}}) \quad (8)$$

$$Q_i = \frac{A_i}{A_{\text{Ref}}} \sin(\varphi_i - \varphi_{\text{Ref}}). \quad (9)$$

The position and tilt signals, P_i and T_i respectively, were

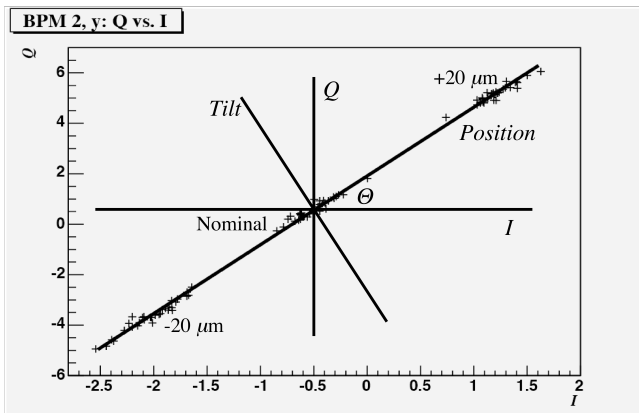


FIG. 13: Q plotted against I (in this case for BPM 2, y). The three clusters of points each contain 32 beam pulses corresponding to three different y positions for BPM 2: The nominal position, and $\pm 20 \mu\text{m}$. The IQ -phase Θ is the angle between the the I - Q basis and the $Position$ - $Tilt$ basis. The point spread in each cluster is due to beam jitter. The center cluster, which corresponds to the nominal y position of BPM 2, is not located at $(0,0)$ owing to a small amount of residual y tilt and y offset for BPM 2.

then a rotation from I_i and Q_i ,

$$\begin{pmatrix} P_i \\ T_i \end{pmatrix} = \begin{pmatrix} \cos \Theta_i & \sin \Theta_i \\ -\sin \Theta_i & \cos \Theta_i \end{pmatrix} \begin{pmatrix} I_i \\ Q_i \end{pmatrix}. \quad (10)$$

where Θ_i was the IQ -phase for channel i . This is illustrated graphically in Figure 13. The quantities x , x' , y , and y' were then proportional to the quantities P and T :

$$x_n \text{ or } y_n = s_i P_i \quad (11)$$

$$x'_n \text{ or } y'_n = s'_i T_i \quad (12)$$

where each of the six different channels i corresponded to x or y for BPM 1, 2, or 3, and where s_i and s'_i were the position and tilt scales respectively.

A. Fitting

In the fitting algorithm, the waveforms from each of the channels i as well as the reference cavity waveform were simply fitted a second time using equation 7; this time, however, only the amplitude A and phase φ were considered as parameters to be determined by the fit.

B. Digital Down-Conversion

In the digital down-conversion (DDC) algorithm, the raw waveform was first multiplied by a local oscillator (LO) of the same frequency ω to yield a zero intermediate frequency (IF) – denoted U , the real and imaginary parts

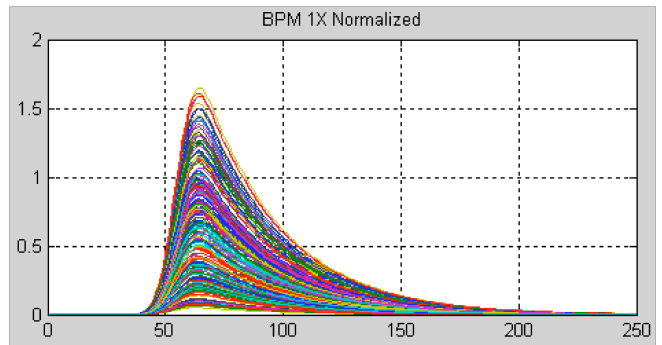


FIG. 14: Demodulated waveforms from BPM 1, x for a data set. Each colored line represents a separate ATF extraction and has been normalized by the corresponding amplitude of the reference cavity. In the plot, the x axis refers to the sample number.

of which were

$$\Re U = (V - V_0) \times \cos(\omega t) \quad (13)$$

$$\Im U = (V - V_0) \times \sin(\omega t). \quad (14)$$

The real and imaginary parts of each IF were then multiplied by a 39 coefficient, symmetric, finite impulse response (FIR), low-pass filter with 2.5 MHz 3 dB bandwidth,

$$\begin{pmatrix} D_1 \\ D_2 \\ \vdots \\ D_{249} \\ D_{250} \end{pmatrix} = \begin{pmatrix} 0 & \cdots & 0 & U_1 & U_2 & \cdots & U_{20} \\ 0 & \cdots & U_1 & U_2 & U_3 & \cdots & U_{21} \\ \vdots & \vdots & \vdots & \vdots & \vdots & \vdots & \vdots \\ U_{229} & \cdots & U_{248} & U_{249} & U_{250} & 0 & \cdots \\ U_{230} & \cdots & U_{249} & U_{250} & 0 & 0 & \cdots \end{pmatrix} \begin{pmatrix} F_1 \\ \vdots \\ F_{39} \end{pmatrix} \quad (15)$$

where here the subscripts on U and D indicate sample number, F denotes the filter vector, and D the demodulated waveform. A series of demodulated waveforms are illustrated in Figure 14.

The amplitude for each channel was defined at a particular time selected to be near the peak of the waveform. If, however, the amplitude could not be evaluated there due to electronic saturation, the amplitude and phase were evaluated at the first non-saturated time and their value at the nominal time was determined by extrapolation using the measured decay constant and frequency.

V. CALIBRATION

To get x , x' , y , and y' from the the raw BPM signals, several parameters had to be known a priori: The IQ -phase Θ had to be known to determine the position P and

tilt T from I and Q for each channel; because P and T had arbitrary units, the position scales s and tilt scales s' had therefore be known to determine x and y in μm and x' and y' in μrad . The calibration procedure described here determined the IQ -phase Θ_i , and the position and tilt scales s_i and s'_i respectively for both the x and y channels of each of the three BPMs in a manner which eliminated the effects of beam jitter.

A. IQ -Phase Determination

For a given transverse direction, x or y , the value of I or Q in any one BPM should be related by a linear equation to the values of I and Q in the other two BPMs since the 1.28 GeV beam travels through the three BPMs in a very nearly straight line:

$$I_i = a_{ij}I_j + b_{ij}Q_j + a_{ik}I_k + b_{ik}Q_k + c_i \quad (16)$$

$$Q_i = f_{ij}I_j + g_{ij}Q_j + f_{ik}I_k + g_{ik}Q_k + h_i \quad (17)$$

where $i, j, k = 1, 2, 3$ and $i \neq j \neq k$. We desired to find the values of the coefficients a , b and c , and f , g and h which would allow us to predict I and Q in one BPM from the values of I and Q in the other two. Repeated application of the above two equations (denoted by ellipses below) for many ATF extractions yielded a set of simultaneous equations which could be expressed in terms of a single matrix equation $\mathbf{b} = \mathbf{A}\mathbf{x}$, where \mathbf{x} was a column vector comprised of the coefficients a , b and c , or f , g and h , \mathbf{b} was a column vector of the measured values for either I or Q from a given BPM, and \mathbf{A} was the matrix of I s and Q s from the other two BPMs. The matrix also contained a column of ones which allowed for a constant term. Each row of \mathbf{A} and \mathbf{b} corresponded to a single ATF extraction:

$$\begin{pmatrix} I_i \\ \vdots \end{pmatrix} = \begin{pmatrix} I_j & Q_j & I_k & Q_k & 1 \\ \vdots & \vdots & \vdots & \vdots & \vdots \end{pmatrix} \begin{pmatrix} a_{ij} \\ b_{ij} \\ a_{ik} \\ b_{ik} \\ c_i \end{pmatrix} \quad (18)$$

$$\begin{pmatrix} Q_i \\ \vdots \end{pmatrix} = \begin{pmatrix} I_j & Q_j & I_k & Q_k & 1 \\ \vdots & \vdots & \vdots & \vdots & \vdots \end{pmatrix} \begin{pmatrix} f_{ij} \\ g_{ij} \\ f_{ik} \\ g_{ik} \\ h_i \end{pmatrix} \quad (19)$$

Once \mathbf{A} and \mathbf{b} were known, the question became how to find the optimal solution to the equation for the coefficients a , b , and c and f , g , and h in \mathbf{x} . We chose the method of singular value decomposition (SVD) to invert the non-square and possibly singular $m \times n$ matrix \mathbf{A} to yield the matrix \mathbf{A}^+ : This method has the property that the solution $\mathbf{x} = \mathbf{A}^+\mathbf{b}$ minimizes the magnitude $|\mathbf{A}\mathbf{x} - \mathbf{b}|$ [8].

Once these coefficients were known, I and Q in one BPM could be predicted from the values of I and Q from

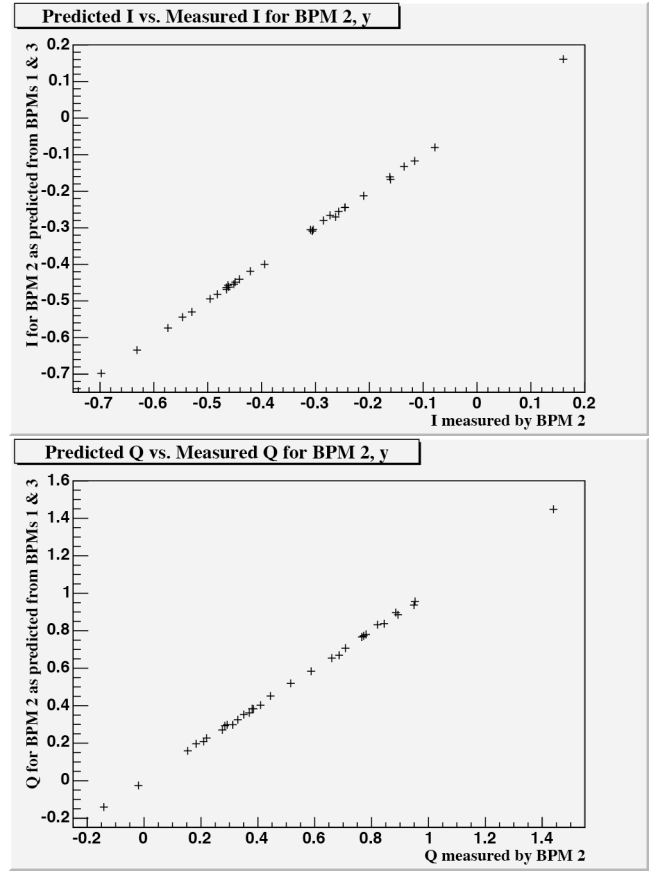


FIG. 15: Calculated values of I (top) and Q (bottom) plotted against the respective measured values (in this case for BPM 2, y). Only ATF extractions with all BPMs in their nominal positions were used in the regressions. Note that the calculated values are highly correlated with the measured values.

the other BPMs for any ATF extraction. This is illustrated in Figure 15. Events where BPM i had been moved were then considered, and ΔI_i and ΔQ_i were defined as the difference between the predicted and measured values for I_i and Q_i respectively: Then

$$\Delta I_i = I_i - (a_{ij}I_j + b_{ij}Q_j + a_{ik}I_k + b_{ik}Q_k + c_i) \quad (20)$$

$$\Delta Q_i = Q_i - (f_{ij}I_j + g_{ij}Q_j + f_{ik}I_k + g_{ik}Q_k + h_i) \quad (21)$$

and any significant deviation from zero of ΔI_i and ΔQ_i was attributed to the change in position of BPM i . For pure translations of BPM i , the values of ΔI_i and ΔQ_i lay along a straight line, as illustrated in Figure 16. ΔQ_i could then be regressed against ΔI_i ,

$$\begin{pmatrix} \Delta Q_i \\ \vdots \end{pmatrix} = \begin{pmatrix} \Delta I_i & 1 \\ \vdots & \vdots \end{pmatrix} \begin{pmatrix} A_i \\ B_i \end{pmatrix} \quad (22)$$

and the IQ -phase was the arctangent of the slope A_i ,

$$\Theta_i = \arctan(A_i). \quad (23)$$

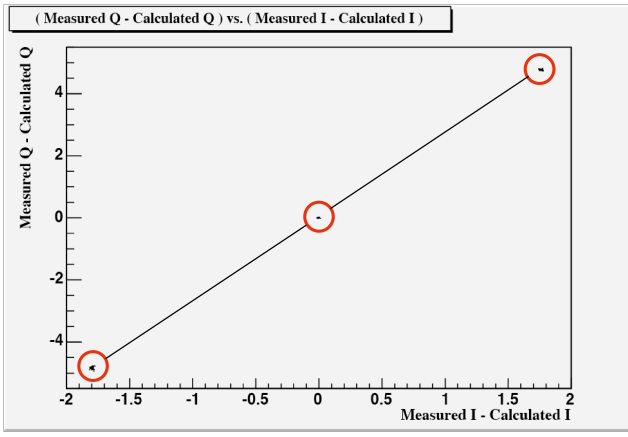


FIG. 16: ΔQ plotted against ΔI (in this case for BPM 2, y). Each of the three tiny blobs (inside the red circles) actually contains 32 ATF extractions.

B. Position Scales

The determination of the position scales s_i began by noting that the trajectory of the beam between BPMs 1 and 2 was the same as that between 2 and 3, irrespective of how the BPMs had been moved. The electrical centers of BPMs 1 and 3, in their nominal positions, were used to define a coordinate axis, and BPM 2 was allowed to have a residual offset with respect to this axis. This is shown schematically in Figure 17, and may be written mathematically as

$$\frac{(m_2 + x_2 + s_2 P_2) - (m_1 + s_1 P_1)}{z_{12}} = \frac{(m_3 + s_3 P_3) - (m_2 + x_2 + s_2 P_2)}{z_{23}} \quad (24)$$

where m_n denotes the amount BPM n has been moved away from its nominal position, and where x_2 denotes the offset of BPM 2 relative to the axis defined by the electrical centers of BPMs 1 and 3. The BPMs were moved one at a time, resulting in four different linearly independent configurations:

$$m_1 = m_2 = m_3 = 0, \quad (25)$$

$$m_1 \neq 0, m_2 = m_3 = 0, \quad (26)$$

$$m_2 \neq 0, m_1 = m_3 = 0, \quad (27)$$

$$m_3 \neq 0, m_1 = m_2 = 0. \quad (28)$$

Repeated application of equation 24 over multiple ATF extractions with the four configurations noted in equations 25 through 28 yielded the matrix equation

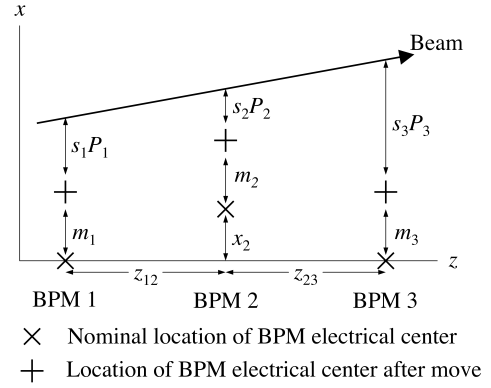


FIG. 17: The nominal positions of the electrical centers of BPMs 1 and 3 define the coordinate system, and BPM 2 is allowed to have a relative offset: These are denoted above with a \times . Each BPMs is then moved in turn away from its nominal position by known a amount m_n . The new position for the electrical center of the BPM is denoted by a $+$. The quantity z_{mn} is the distance between BPMs along the beamline.

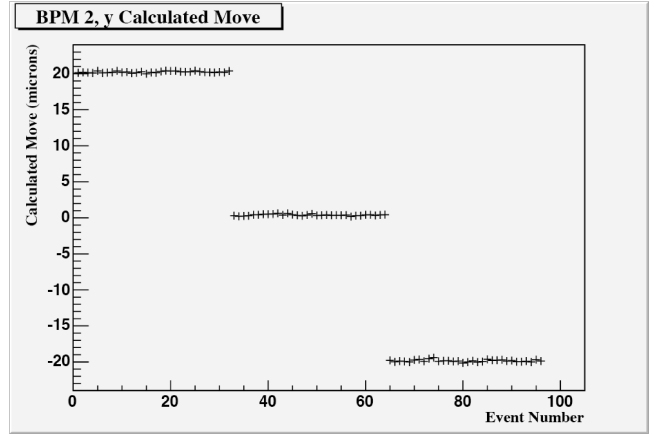


FIG. 18: Once x_2 and s_n had been determined, the amount by which any BPM had been moved could be calculated as a means of verifying the calibration. This plot shows the calculated move for the 96 events over which BPM 2, y was being moved, and clearly shows the pattern used: Nominal location plus 20 μm , nominal location, and nominal location minus 20 μm .

$$\begin{pmatrix} \frac{m_1}{z_{12}} - \frac{m_2}{z_{12}+z_{23}} + \frac{m_3}{z_{23}} \\ \vdots \end{pmatrix} = \begin{pmatrix} \frac{1}{z_{12}+z_{23}} & -\frac{P_1}{z_{12}} & \frac{P_2}{z_{12}+z_{23}} & -\frac{P_3}{z_{23}} \\ \vdots & \vdots & \vdots & \vdots \end{pmatrix} \begin{pmatrix} x_2 \\ s_1 \\ s_2 \\ s_3 \end{pmatrix} \quad (29)$$

The result of inverting this matrix using the technique of singular value decomposition allowed x_2 and s_n to be determined.

The calibration could be verified by using x_2 and s_n

to calculate the amount each BPM had supposedly been moved, and this result compared to the amount the BPM was actually moved. This comparison is shown in Figure 18.

C. Tilt Scales

In one respect, the tilt signals were more difficult to calibrate because there was no way to separate the contribution to the tilt signal due to the angle of obliquity of the beam from that due to the angle of attack of the bunch (both relative to the orientation of the cavity). However, the trajectory of the beam could be independently determined from its positions registered in the other two BPMs, and this in turn could be related to the angle of obliquity by a constant θ_{0i} which was the nominal orientation of the cavity relative to the electrical centers of the other two BPMs. The average angle of attack over a series of ATF extractions was assumed to be nearly constant, or in any case fluctuations in the average were assumed to be small compared to the other terms, most notably the tilt t_i of the BPM as applied by the movers. For a given BPM, the trajectory of the beam as determined from the position signals in the other two BPMs was taken as equal to the sum of θ_{0i} , the angle of applied tilt of the BPM t_i , and the scaled tilt signal $s'_i T_i$ (neglecting the bunch's angle of attack). This is illustrated schematically in Figure 19, and may be written mathematically as

$$\frac{x_k - x_j}{z_{jk}} = s'_i T_i + \theta_{0i} + t_i \quad (30)$$

As with the position calibration, the BPMs were moved one at a time, resulting in four different configurations:

$$t_1 = t_2 = t_3 = 0, \quad (31)$$

$$t_1 \neq 0, t_2 = t_3 = 0, \quad (32)$$

$$t_2 \neq 0, t_1 = t_3 = 0, \quad (33)$$

$$t_3 \neq 0, t_1 = t_2 = 0. \quad (34)$$

Repeated application of equation 30 over multiple ATF extractions with the four configurations noted in equations 31 through 34 yields the matrix equation

$$\begin{pmatrix} \frac{x_k - x_j}{z_{jk}} - t_i \\ \vdots \end{pmatrix} = \begin{pmatrix} T_i & 1 \\ \vdots & \vdots \end{pmatrix} \begin{pmatrix} s'_i \\ \theta_{0i} \end{pmatrix}. \quad (35)$$

The matrix may be inverted using the technique of singular value decomposition to determine s'_i and θ_{0i} . Unlike the position calibration procedure, the tilt calibrations of the separate BPMs are uncoupled.

The calibration could be verified by using θ_{0i} and s'_i to calculate the amount each BPM had supposedly been tilted, and this result could then be compared with the amount the BPM was actually tilted. This comparison is shown in Figure 20.

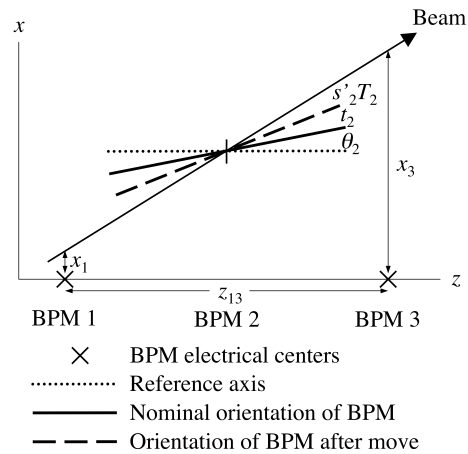


FIG. 19: When calibrating the tilt scales s'_i for a given BPM, the electrical centers of the other two BPMs define the coordinate system. The beam's trajectory is determined relative to this coordinate system by the position signals in those two BPMs. The nominal orientation of the BPM in question relative to this coordinate system θ_{0i} , the applied tilt t_i , and the scaled tilt signal $s'_i T_i$, added together, should equal the beam trajectory, as illustrated.

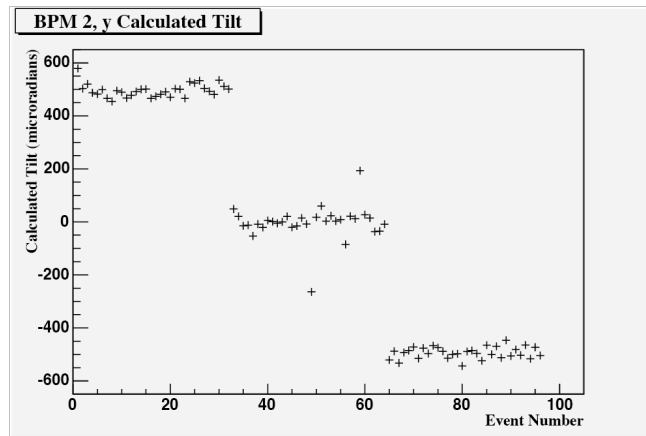


FIG. 20: Once θ_{0i} and s'_i have been determined, the amount by which the BPM has been tilted may be calculated as a means of verifying the calibration. This plot shows the calculated tilts for the 96 events over which BPM 2, y was being tilted, and clearly shows the pattern used: Nominal orientation plus 500 μ radians, nominal orientation, and nominal orientation minus 500 μ radians. Deviations from the applied tilts may be attributed to jitter in the bunch's angle of attack.

VI. BPM RESOLUTION

BPM resolution was determined by measuring the residual – that is the difference between the predicted position, as calculated from the beam's position in the other two BPMs, and the measured position of the beam in the BPM in question. This is illustrated in figure 21.

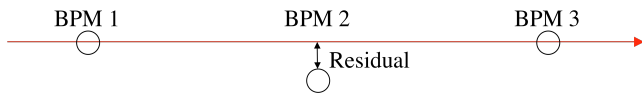


FIG. 21: The residual is the difference between the position of the beam measured by a given BPM and the position predicted from the other two BPMs. In this illustration, the circles represent the location of the beam measured by each BPM; the red line represents the beam's trajectory. In this case, the beam's trajectory is defined by its position in BPMs 1 and 3, and the residual is relative to the measured position in BPM 2.

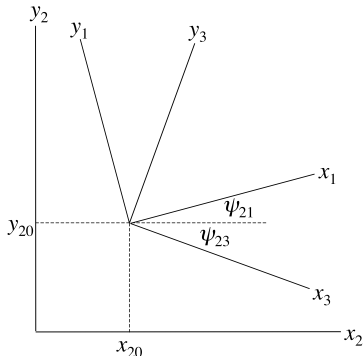


FIG. 22: Let the axis defined by the electrical centers of BPMs 1 and 3 be the origin in the xy planes of all three BPMs: The coordinates associated with BPM 2 are then translated by an offset (x_{20}, y_{20}) . Further, let the orientation of the x and y axes of BPM 2 define the principle axes of the coordinate system: The orientations of the BPMs 1 and 3 will then be rotated relative to BPM 2 by angles ψ_{21} and ψ_{23} , respectively.

The resolution was then proportional to the width of the distribution of the residuals over many ATF extractions.

Because the ATF damping ring involves bends and kickers which operate in the xz plane, the transverse stability of the beam was significantly worse in the x direction. The electronics used to process the BPM signals were thus attenuated in channels corresponding to the x direction so that the electronics would not be overwhelmed by the large signals which were possible. The longest lever arm for constraining the beam's trajectory was that between BPMs 1 and 3. These two facts conspired to make BPM 2, y the channel of choice for measuring the resolution.

In the right coordinate system, as detailed in Figure 22, the y position of the beam in BPM 2 could be related in a straight-forward way to the x and y positions of the beam in BPMs 1 and 3 by the equation

$$y_2 = y_{20} + \frac{z_{12}}{z_{13}} [-\sin(\psi_{21})x_1 + \cos(\psi_{21})y_1] + \frac{z_{23}}{z_{13}} [-\sin(\psi_{23})x_3 + \cos(\psi_{23})y_3]. \quad (36)$$

where y_{20} was the y offset of BPM 2 from the axis defined by the electrical centers of BPMs 1 and 3, ψ_{21} and ψ_{23} were the rotations about the z axis of BPMs 1 and 3 relative to BPM 2, and where z_{mn} was the distance along z between BPMs m and n .

To the degree that the coupling slots for x and y were not orthogonal ($\beta - \alpha \neq 0$ in Figure 37d), x_2 was correlated with y_2 . To see this, consider the limiting case where the x and y coupling slots are parallel to each other (i.e. $\beta - \alpha = 90^\circ$); then $x_2 = y_2$ and the parameters associated with the other two BPMs become irrelevant. It was therefore important to exclude x_2 from the regression because its inclusion could artificially reduce the measured resolution. In any case, x_2 was unnecessary because its value was constrained by x_1 and x_3 .

Equation 36 may be written simply as

$$y_2 = a_2 + b_{21}x_1 + c_{21}y_1 + b_{23}x_3 + c_{23}y_3. \quad (37)$$

Repeated application of equation 37 over many ATF extractions yielded the matrix equation

$$\begin{pmatrix} y_2 \\ \vdots \end{pmatrix} = \begin{pmatrix} 1 & x_1 & x_3 & y_1 & y_3 \\ \vdots & \vdots & \vdots & \vdots & \vdots \end{pmatrix} \begin{pmatrix} a_2 \\ b_{21} \\ b_{23} \\ c_{21} \\ c_{23} \end{pmatrix}. \quad (38)$$

Taking for y_2 the measured values, the coefficients a , b , and c were determined by inverting the matrix using the method of singular value decomposition. These coefficients could be determined using either the entire data sample for a run period or a subset of the data. Once the coefficients had been determined, the residual was calculated as

$$\delta y_2 = y_2 - (a_2 + b_{21}x_1 + c_{21}y_1 + b_{23}x_3 + c_{23}y_3) \quad (39)$$

Other terms could be added to equation 37 to include additional parameters in the determination of y_2 . Such parameters could include x'_1 , y'_1 , x'_3 , and y'_3 . Other possible parameters included beam energy or BPM temperature – indeed any parameter which could be correlated with y_2 .

The resolution R_{2y} was then calculated by dividing the standard deviation of the residual distribution by a geometric weight factor,

$$R_{2y} = \frac{\sqrt{\langle(\delta y_2)^2\rangle - \langle\delta y_2\rangle^2}}{\sqrt{(\frac{1}{2})^2 + 1^2 + (\frac{1}{2})^2}} \quad (40)$$

VII. RESULTS

We present here the results from two data sets, the first taken on the evening of 11 March, 2005, and the second taken during the day on 27 May, 2005.

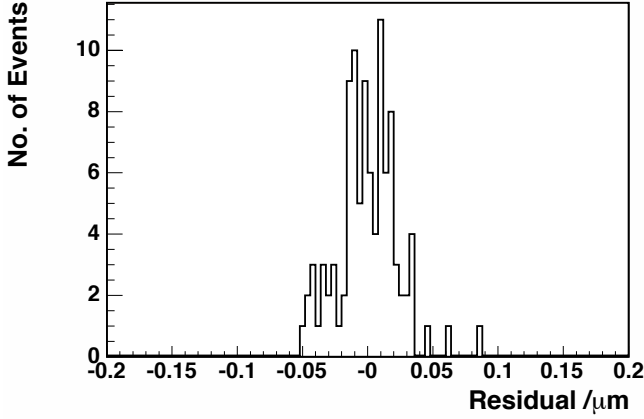


FIG. 23: The residuals δy_2 for 100 ATF extractions from 27 May 2005. This data was analyzed using the fitting algorithm.

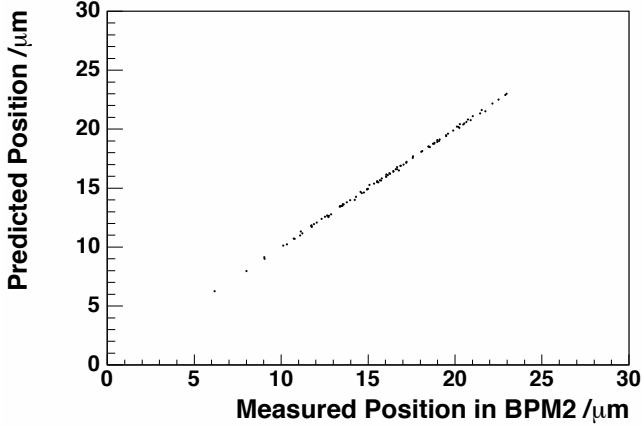


FIG. 24: The beam position at BPM 2 as predicted by BPMs 1 and 3 vs. the measured position in BPM 2 for 100 ATF extractions from 27 May 2005. This data was analyzed using the fitting algorithm.

A. Resolution on Short Time Scales

Figure 23 shows the distribution of the residuals for 100 ATF extractions from 27 May, 2005. This small data set spanning a period of roughly a minute and a half yielded among the best resolutions achieved to date using the fitting algorithm:

$$R_{2y} = \frac{23.1 \text{ nm}}{\sqrt{3/2}} = 18.9 \text{ nm}. \quad (41)$$

Figure 24 shows the correlation between the predicted position and the measured position, the difference of which is the residual.

Figure 25 shows the residuals plotted against beam po-

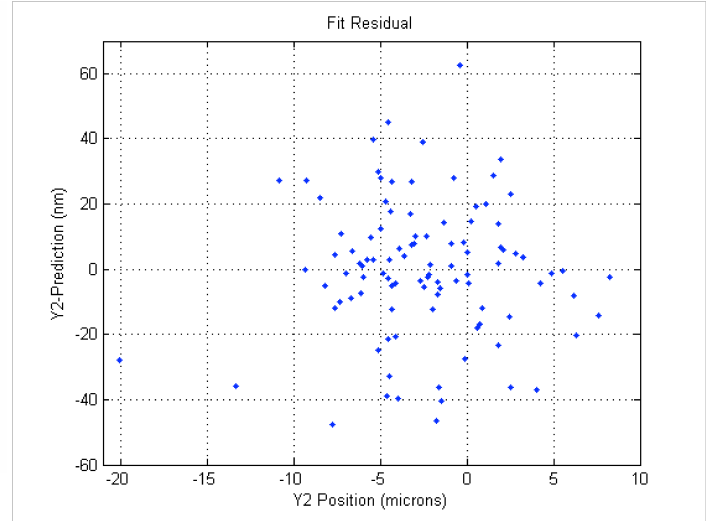


FIG. 25: The residual δy_2 for BPM 2 vs. the position in BPM 2, y for 100 ATF extractions from 27 May 2005. This data was analyzed using the digital down-conversion (DDC) algorithm, and the calculation of the predicted position included terms for x'_1 , y'_1 , x'_3 , and y'_3 .

sition in BPM 2, y for 100 ATF extractions from 27 May, 2005. This small data set spanning a period of roughly a minute and a half yielded among the best resolutions achieved to date using the digital down-conversion (DDC) algorithm. The calculation of the residual in this case added additional terms for x'_1 , y'_1 , x'_3 , and y'_3 to equations 37 through 39:

$$R_{2y} = \frac{20.8 \text{ nm}}{\sqrt{3/2}} = 17.0 \text{ nm}. \quad (42)$$

Figure 26 shows the correlation between the predicted position and the measured position, the difference of which is the residual.

B. Resolution over Longer Time Scales

Figure 27 shows the distribution of the residuals δy_2 for 800 ATF extractions from 27 May 2005. This data set was analyzed using the digital down-conversion algorithm and the calculation of the residual in this case added additional terms for x'_1 , y'_1 , x'_3 , and y'_3 to equations 37 through 39. The data here covered a roughly 10 minute time period and demonstrated that high resolution was achievable over longer time periods as well. The distribution in Figure 27 yielded a resolution of

$$R_{2y} = \frac{29.4 \text{ nm}}{\sqrt{3/2}} = 24.0 \text{ nm}. \quad (43)$$

Plotting the residual against time showed that the fluctuations in the residual remained fairly constant across

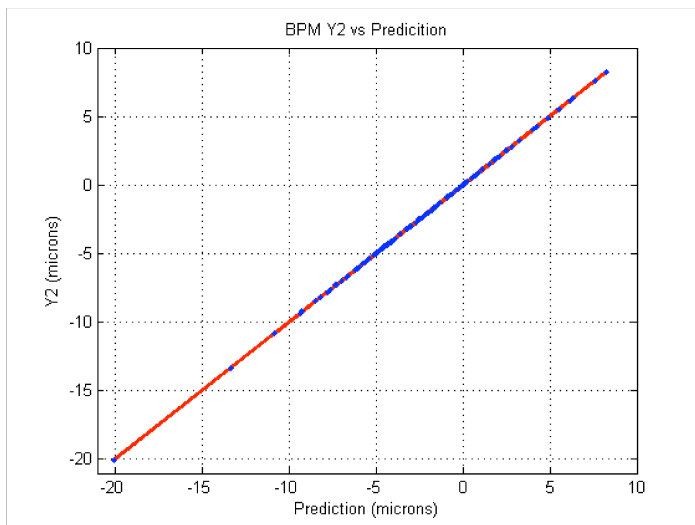


FIG. 26: The measured position vs. the predicted position for BPM 2 for 100 ATF extractions from 27 May 2005. This data was analyzed using the digital down-conversion (DDC) algorithm, and the calculation of the predicted position included terms for x'_1 , y'_1 , x'_3 , and y'_3 .

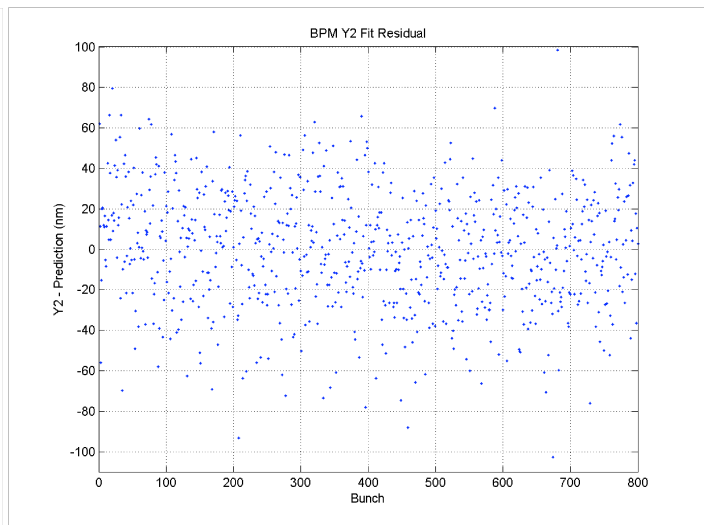


FIG. 28: The residual for BPM 2 vs. the event number (equivalent to time) for 800 ATF extractions from 27 May 2005. This data was analyzed using the digital down-conversion (DDC) algorithm, and the calculation of the predicted position included terms for x'_1 , y'_1 , x'_3 , and y'_3 . The lack of structure here demonstrates the stability of the experiment.

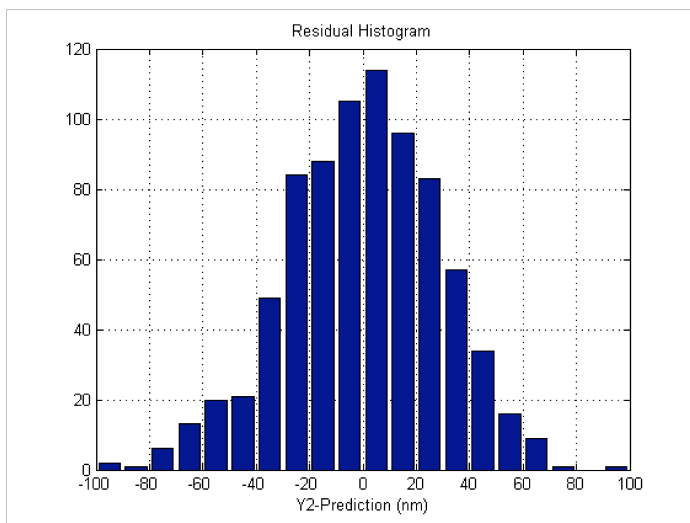


FIG. 27: The residual δy_2 for 800 ATF extractions from 27 May 2005. This data was analyzed using the digital down-conversion (DDC) algorithm, and the calculation of the predicted position included terms for x'_1 , y'_1 , x'_3 , and y'_3 .

the entire time span – note the lack of structure in Figure 28. This was in sharp contrast to the obvious structure which appeared when the beam position was plotted against time, as shown in Figure 29: The beam clearly drifted over the period of data taking. But despite movements of the beam, the residual remained stable.

Figure 30 shows the distribution of the residuals δy_2 for 2300 ATF extractions from the evening of 11 March 2005. Four events were removed on account of having a low

reference cavity amplitude and a further two flier events were removed for a total of 2294 events. This data set covered a much longer time period of order half an hour and demonstrated that high resolution was achievable over very long time periods as well. The distribution in Figure 30 yields a resolution of

$$R_{2y} = \frac{28.9 \text{ nm}}{\sqrt{3/2}} = 23.6 \text{ nm}. \quad (44)$$

Figure 31 shows the correlation between the predicted position and the measured position, the difference of which is the residual. Plotting the residual against time showed that the fluctuations in the residual remained fairly constant across the entire time span – note the lack of structure in Figure 32. This was in sharp contrast to the obvious structure which appeared when the beam position was plotted against time, as shown in Figure 33: The beam clearly drifted over the period of data taking. But despite movements of the beam, the residual remained stable.

VIII. OTHER EFFECTS

A. t_0 Reference Point

Nominally, the parameter t_0 was calculated by fitting the rise of the signal from the crystal detector, and defining t_0 to be at the midpoint of the rise, i.e. the time corresponding to when the signal was 0.5 times the value at the peak. This was detailed in Figure 12. However, the

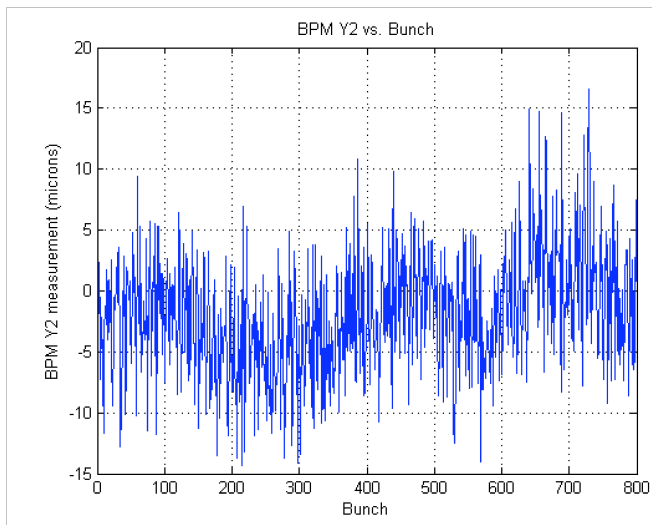


FIG. 29: The beam position measured in BPM 2 vs. the event number (equivalent to time) for 800 ATF extractions from 27 May 2005. This data was analyzed using the digital down-conversion (DDC) algorithm, and the calculation of the predicted position included terms for x'_1 , y'_1 , x'_3 , and y'_3 . The structure shown here illustrates the beam drifts which occurred during the period of data taking.

seven channels did not have precisely the same resonant frequencies, which fact could introduce phase errors – most notably between the reference cavity and the other channels. By varying the fraction of the peak of the crystal detector signal used as the reference point at which t_0 was defined, we could study its effect on the resolution and thereby hope to minimize any adverse effect on resolution. Figure 34 shows how the standard deviation of the residuals – which is proportional to the resolution – is effected by varying the t_0 reference point in the data for 2300 ATF extractions taken on the evening of 11 March 2005. Defining t_0 to be at 0.6 of the peak of the crystal detector signal improved the resolution only minimally: R_{2y} goes to 23.52 nm from 23.60 nm.

B. Magnetic Fields

A magnetic field having an x component (in the coordinates of the beam) will cause the beam to assume a curved trajectory in the yz -plane as it passes through the three BPMs. If the sagitta is constant, the measurement of the resolution is unaffected and is taken into account by the constant term y_{20} in equation 36. However, the presence of such a magnetic field can have an effect on the measured resolution in two ways: Changes in either the beam's energy or the strength of the magnetic field will cause changes in the radius of the curvature of the beam's trajectory and thus to the sagitta. The sagitta δ

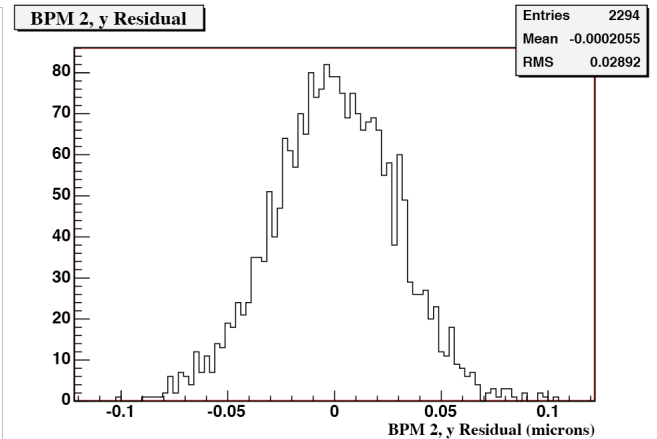


FIG. 30: The residuals δy_2 for 2300 ATF extractions from a period spanning approximately half an hour on the evening of 11 March 2005. Four events were removed on account of low reference cavity amplitude, which usually signifies either a missing bunch or at least a very low current bunch, and a further two flier events were removed for a total of 2294 events. The coefficients used to calculate the residuals were determined from the entire data set less the low reference cavity amplitude events.

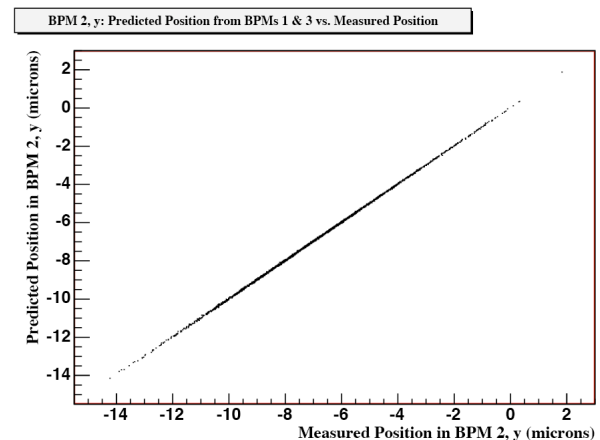


FIG. 31: The beam position at BPM 2 as predicted by BPMs 1 and 3 vs. the measured position in BPM 2 for 2300 ATF extractions from the evening of 11 March 2005. Four events were removed on account of low reference cavity amplitude, which usually signifies either a missing bunch or at least a very low current bunch, and a further two flier events were removed for a total of 2294 events. The coefficients used to calculate the position at BPM 2 from the positions in BPMs 1 and 3 were determined from the entire data set.

may be calculated as

$$R(\text{cm}) = \frac{1}{c \times 10^{-17}} \times \frac{p(\text{GeV}/c)}{B_{\perp}(\text{gauss})}, \quad (45)$$

$$\sin \theta = \frac{L}{2R}, \quad (46)$$

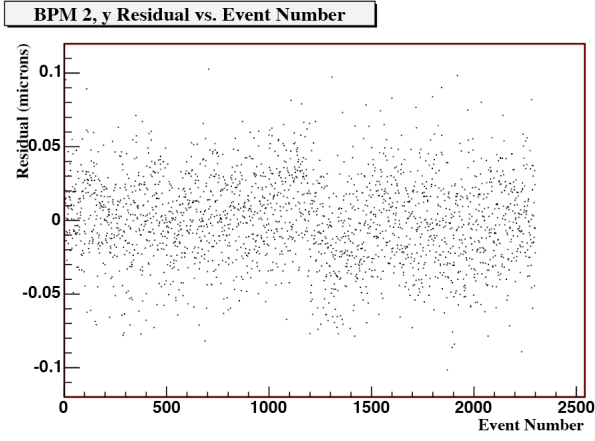


FIG. 32: The residual for BPM 2 vs. the event number (equivalent to time) for the 2300 ATF extractions from the evening of 11 March 2005. Four events were removed on account of low reference cavity amplitude, which usually signifies either a missing bunch or at least a very low current bunch, and a further two flier events were removed. The lack of structure here demonstrates the stability of the experiment.

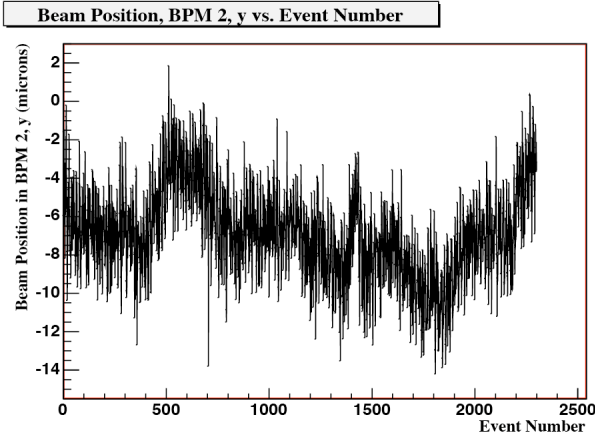


FIG. 33: The beam position measured in BPM 2 vs. the event number (equivalent to time) for the 2300 ATF extractions from the evening of 11 March 2005. Four events were removed on account of low reference cavity amplitude, which usually signifies either a missing bunch or at least a very low current bunch, and a further two flier events were removed. The structure shown here illustrates the beam drifts which occurred during the period of data taking.

$$z = \frac{L}{2 \tan \theta}, \quad (47)$$

$$\delta = R - z. \quad (48)$$

and is shown schematically in Figure 35.

The earth's magnetic field at the ATF on 11 March 2005 was determined to have a total intensity of 46,430.02 nT, changing by -14.22 nT per year [12]. For

$$p = 1.28 \text{ GeV}/c,$$

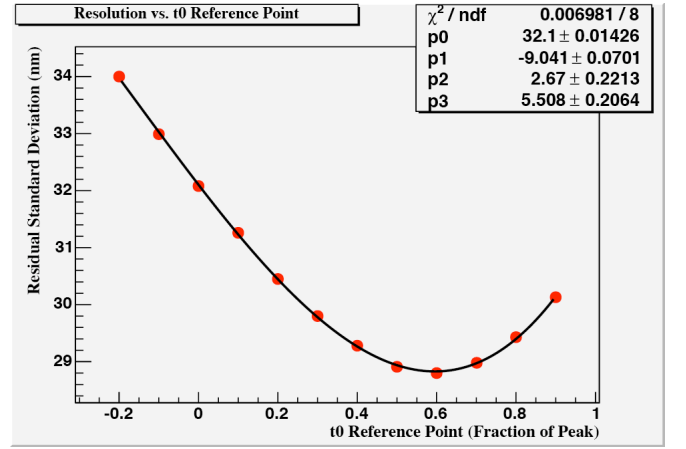


FIG. 34: The standard deviation of the residuals (proportional to the resolution) is plotted against the fraction of the peak of the crystal detector signal used as the reference point at which t_0 is defined; i.e. the number 0.5 in Figure 12 is varied to determine how the resolution changes. This data fits to a third-order polynomial of the form $y = \sum_n p_n x^n$ with the coefficients shown, and the minimum is at 0.596.

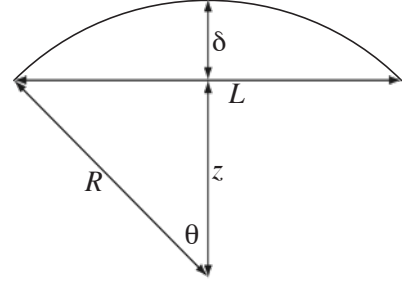


FIG. 35: The sagitta of the beam due to a magnetic field orthogonal to the beam.

$$L = 60 \text{ cm},$$

$$B_{\oplus} = .46430 \text{ gauss},$$

the radius of curvature of the trajectory R and sagitta δ were

$$R = 3.33 \times 10^6 \text{ cm}$$

$$\delta = 489 \text{ nm}$$

The stability of the beam energy was investigated by using the measured position of the beam from the 52 BPMs in the ATF arcs:

$$\frac{\Delta E}{E} = \frac{1}{N} \sum_{\text{ATF BPMs}} \frac{x_i - \langle x_i \rangle}{\eta_i}, \quad (49)$$

where η_i was the design dispersion for BPM i and $\langle x_i \rangle$ for a given event was calculated from the average position in

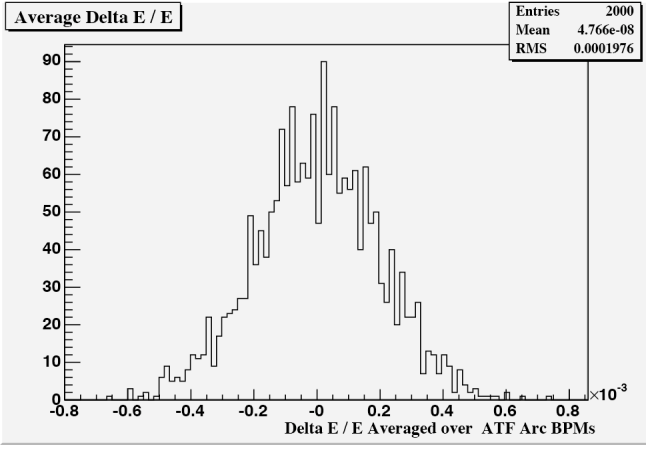


FIG. 36: Estimate of the fractional variation in the beam energy. The average is taken over the 52 BPMs in the ATF arcs.

BPM i of 40 events surrounding the event in question:

$$\langle x_i \rangle = \frac{1}{40} \sum_{n=\text{event}-20}^{\text{event}+20} x_{in}. \quad (50)$$

The distribution in Figure 36 is in excellent agreement with the design energy stability of the ATF.

The stability of the beam energy and the fluctuations of the earth's magnetic field had the following affects on the sagitta and by extension the measured resolution of the BPMs:

$$\frac{\Delta p}{p} = .0002 \rightarrow \Delta \delta = 0.07 \text{ nm}$$

$$\frac{\Delta B}{B} = \frac{14}{46430} \rightarrow \Delta \delta < 0.15 \text{ nm}$$

The figure for $\Delta B/B$ should be considered as an upper limit as the worst-case scenario was assumed – namely that the orientation of the earth's magnetic field was perpendicular to the beam.

C. Temperature

Five temperature sensors, distributed among the mounting rings and the hexapod strut movers, were associated with each BPM. The data from these sensors was read out on a run by run (as opposed to an event by event) basis. No correlation was seen between this data and the residual δy_2 and no improvement in the residual was found when this data was added as an additional parameter to equations 38 and 39.

D. Cross Talk

If the BPMs are not perfectly machined but rather the cavities have a degree of eccentricity, excitations of

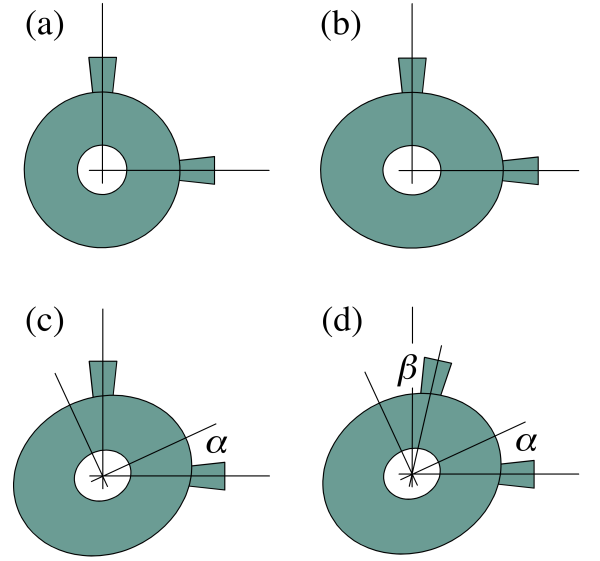


FIG. 37: (a) A perfectly circular cavity with the wave guides at right angles. (b) An elliptical cavity with the semi-major and semi-minor axes aligned with the wave guides. (c) An elliptical cavity with the semi-major and semi-minor axes rotated by an angle α relative to the wave guides. (d) An elliptical cavity with the semi-major and semi-minor axes rotated by an angle α relative to the x -wave guide and by an angle β relative to the y -wave guide.

the cavities' antisymmetric modes in the x direction may become coupled with those in the y direction. In a perfectly round cavity, as shown in Figure 37 (a), the x and y antisymmetric modes are degenerate:

$$X = X_0 + A_x e^{-\Gamma(t-t_0)} \sin[\omega(t-t_0) + \varphi_x], \quad (51)$$

$$Y = Y_0 + A_y e^{-\Gamma(t-t_0)} \sin[\omega(t-t_0) + \varphi_y], \quad (52)$$

where X_0 and Y_0 are the pedestal values for the signals from the x and y channels, respectively. If the cavity has a non-zero eccentricity, as shown in Figure 37 (b), but the waveguides are aligned with the semi-major and semi-minor axes, the x and y antisymmetric modes become non-degenerate:

$$X = X_0 + A_x e^{-\Gamma_x(t-t_0)} \sin[\omega_x(t-t_0) + \varphi_x], \quad (53)$$

$$Y = Y_0 + A_y e^{-\Gamma_y(t-t_0)} \sin[\omega_y(t-t_0) + \varphi_y]. \quad (54)$$

If, however, the waveguides are not aligned with the semi-major and semi-minor axes, as shown in Figure 37 (c), the antisymmetric modes of x and y can mix:

$$X = X_0 + \cos(\alpha) A_x e^{-\Gamma_x(t-t_0)} \sin[\omega_x(t-t_0) + \varphi_{xx}] + \sin(\alpha) A_y e^{-\Gamma_{xy}(t-t_0)} \sin[\omega_y(t-t_0) + \varphi_{xy}], \quad (55)$$

$$Y = Y_0 - \sin(\alpha) A_x e^{-\Gamma_x(t-t_0)} \sin[\omega_x(t-t_0) + \varphi_{yx}] + \cos(\alpha) A_y e^{-\Gamma_y(t-t_0)} \sin[\omega_y(t-t_0) + \varphi_{yy}]. \quad (56)$$

The situation is only slightly more complex if the waveguides are not perfectly orthogonal to each other, as shown

in Figure 37 (d),:

$$X = X_0 + \cos(\alpha)A_x e^{-\Gamma_x(t-t_0)} \sin[\omega_x(t-t_0) + \varphi_{xx}] \\ + \sin(\alpha)A_y e^{-\Gamma_y(t-t_0)} \sin[\omega_y(t-t_0) + \varphi_{xy}], \quad (57)$$

$$Y = Y_0 - \sin(\beta)A_x e^{-\Gamma_x(t-t_0)} \sin[\omega_x(t-t_0) + \varphi_{yx}] \\ + \cos(\beta)A_y e^{-\Gamma_y(t-t_0)} \sin[\omega_y(t-t_0) + \varphi_{yy}]. \quad (58)$$

We explicitly looked for cross talk between the x and y modes by trying to fit the raw waveforms to an equation of the form of equations 57 and 58 (see Figure 37d). To date, no conclusive evidence of crosstalk has been found.

IX. BPM OUTPUT SIGNALS AND RESOLUTION

A. Energy in a Cavity

The exchange of energy between the beam and the cavity depends entirely on the geometry of the cavity and the properties of the bunch rather than on the cavity material. It can be characterized by the normalized shunt impedance

$$\frac{R}{Q} = \frac{V^2}{\omega U}, \quad (59)$$

where V is the integral of E_z in the cavity along the beam trajectory, ω is the resonant frequency, and U is the energy stored in the cavity, all calculated for the mode of interest of the cavity – usually the TM_{110} mode whose excitation depends on the beam's trajectory. The shunt impedance is a function of the beam's trajectory because the voltage V excited in the cavity is proportional to the transverse offset of the beam relative to the electrical center of the cavity.

The energy left in the cavity after a short bunch of charge q passes through it can be calculated as [9]

$$W = \frac{\omega R}{4 Q} q^2. \quad (60)$$

and is proportional to the square of the beam offset. By comparison, a gaussian distributed bunch of length σ leaves less energy in the cavity when σ is comparable to or larger than the wavelength of the dipole mode oscillations. This fact leads to a modification of equation 60, [7]

$$W = \frac{\omega R}{4 Q} q^2 e^{-\frac{\omega^2 \sigma^2}{c^2}}, \quad (61)$$

where c is the speed of the light (we assume the bunch to be relativistic).

The external quality factor of the cavity describes the strength of the cavity coupling to the outer network, and may be expressed as

$$Q_{\text{ext}} = \frac{\omega U}{P_{\text{out}}}. \quad (62)$$

Only a portion of the energy in equation 61 proportional to $1/Q_{\text{ext}}$ will be coupled out of the cavity. The output power coming from the cavity just after the excitation is

$$P_{\text{out}} = \frac{\omega^2 R}{4 Q_{\text{ext}} Q} q^2 e^{-\frac{\omega^2 \sigma^2}{c^2}}, \quad (63)$$

assuming a small change in P_{out} over a cycle.

The voltage in an output line with impedance Z is

$$V_{\text{out}} = \sqrt{P_{\text{out}} Z} = \frac{\omega}{2} \sqrt{\frac{Z R}{Q_{\text{ext}} Q}} e^{-\frac{\omega^2 \sigma^2}{2c^2}} q. \quad (64)$$

As the energy stored in the cavity decays, the output power also decays. It is important to include here both the power going into the output network as well as the power dissipated in the cavity walls. The latter term depends on the wall material and is described by the internal quality factor Q_0 . The decay is exponential with a decay constant τ which may be written as

$$\tau = \frac{2Q_L}{\omega} \quad (65)$$

where

$$\frac{1}{Q_L} = \frac{1}{Q_0} + \frac{1}{Q_{\text{ext}}}. \quad (66)$$

and where the internal quality factor is

$$Q_0 = \frac{\omega U}{P_{\text{diss}}}. \quad (67)$$

Most of the energy stored in the cavity decays over this time period. By the same reasoning, most of the energy coupled out of the cavity is also contained in the same time period. We can determine this energy by integrating the output power,

$$W_{\text{out}} = \int_0^\tau P_{\text{out}} e^{-\frac{t}{\tau}} dt = P_{\text{out}} \tau \left(1 - \frac{1}{e}\right). \quad (68)$$

In order to get a realistic estimation of the cavity output, the BPMs were simulated using electromagnetic fields simulation code GdfidL [10]. Basic cavity parameters like resonant frequencies and shunt impedances needed for the calculation of the output power were estimated. The results are listed in Table I.

The output energy, equation 68, normalized by the beam offset and the bunch charge is also known as the loss factor. This value characterizes the sensitivity of the system for a given geometry and material of the cavity. The loss factor for the BINP cavities was extracted from the measured data: The cavities were calibrated such that a beam offset x for a bunch with a charge q corresponded to a known voltage V_x at the output of the downconversion electronics. The loss factor was then given by

$$k_{\text{loss}} = \left(\frac{V_x}{x}\right)^2 \frac{\tau}{GZq^2}, \quad (69)$$

Parameter	TM ₀₁₀	TM ₁₁₀
Resonant frequency, GHz	4.4	6.4
Shunt impedance, Ω	106	1.24 @ 1 mm
Internal quality factor	8390	9810
External quality factor	$\rightarrow \infty$	25970
P_{out} , 8 mm long bunch, $W \text{ mm}^{-2} \text{ C}^{-2}$	-	$6.12 \cdot 10^{16}$
W_{out} over decay time τ , $J \text{ mm}^{-2} \text{ C}^{-2}$	-	$1.23 \cdot 10^9$

TABLE I: Simulated parameters of the BINP BPMs

where G was the gain of the electronics and Z was the coaxial line impedance – 50 Ω in our case.

The calculation of the loss factor included only signals caused by the position of the beam in the cavity, and excluded signals from any tilt that the beam may have had. This also removed a feature in which the loss factor could appear to tend towards infinity at small offsets; the residual signal from the beam tilt would be divided by zero position. The position signal was proportional to the amplitude of the rotated in-phase component of the waveform. As the magnitude of the signal remained constant under this rotation, the voltage due to the beam position was related to the total signal by

$$V_x = \frac{I \cos \Theta + Q \sin \Theta}{\sqrt{I^2 + Q^2}} V_{\text{RMS}}. \quad (70)$$

The loss factor was normalised by the charge of each bunch as determined by the amplitude of the monopole mode signal in the reference cavity. This was calibrated from the ATF bunch charge data included in runs from 1st-3rd June. (As the ATF current monitor data was not thought to be synchronised with the BPMs' data, the average amplitude over each 100 pulses was used.)

The gain in each channel was measured by feeding a local oscillator signal of a well known level into the electronics in place of the BPM output. The frequency of the signal was adjusted to match that of the cavity, in order to pass correctly through the filters and mixers. Given a power input of -76 dBm, the amplitude of the digitised signal was measured to determine the gain. As the power meter could not measure a value this low, the power was measured at a higher value, and reduced by a known amount using attenuators before being passed to the electronics. Results are shown in Table III.

The resulting loss factors for all 6 BPM channels are shown in Fig 38 and Table II. The results were close to $1.23 \cdot 10^9 \text{ J C}^{-2} \text{ mm}^{-2}$ predicted by the theory (another estimation done by Zenghai Li of SLAC predicted $1.37 \cdot 10^{10} \text{ J C}^{-2} \text{ mm}^{-2}$) but some differed by a factor of 3 from the prediction. This could be explained by a shorter real length of the bunch than the 8 mm used for the estimations.

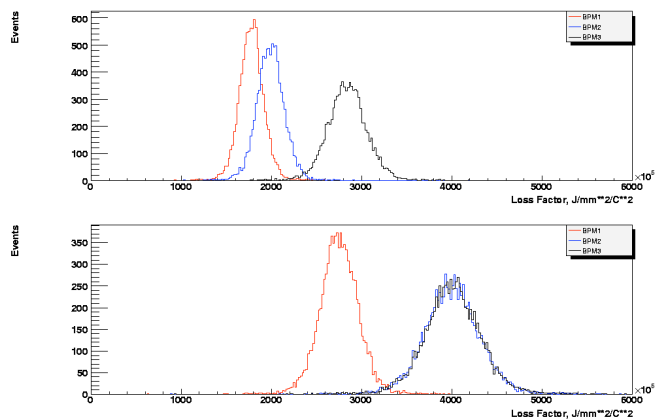


FIG. 38: Measured loss factors in the x (top) and y (bottom) directions from the data measured on 27/05/05. See Table II for explicit values.

B. Noise in the system

Two sources of noise were found to be limiting the achievable BPM resolution, thermal/electronic noise and phase noise. Both were analysed and measured allowing their affect on the BPM resolution to be predicted and improvements proposed.

1. Thermal and Electronic Noise Figure

The signal processing electronics both amplified and contributed to the thermal noise present in the output of the BPMs. This noise could be seen in the recorded waveforms as random voltage variations around the pedestal value, as shown in Figure 39, top plot. The power spectrum of this noise, shown in Figure 39, bottom plot, was found to be flat with an increase over a 20 MHz bandwidth around the final mixdown frequency. This corresponded to the tightest bandpass filter present in the signal processing electronics.

The thermal noise power P of a system is given by

$$P = kT\Delta f \quad (71)$$

where k is Boltzmann's constant, T is the operating temperature, and Δf is the noise bandwidth. Assuming an operating temperature of 293 K and a bandwidth of 20 MHz (defined by the tightest filter in the system) gave a thermal noise power at the BPM output of -100.9 dBm.

		1	2	3
BINP	x	1.78	1.99	2.84
$\times 10^9 \text{ J C}^{-2} \text{ mm}^{-2}$	y	2.75	4.00	4.01

TABLE II: Measured loss factors for the BINP cavities.

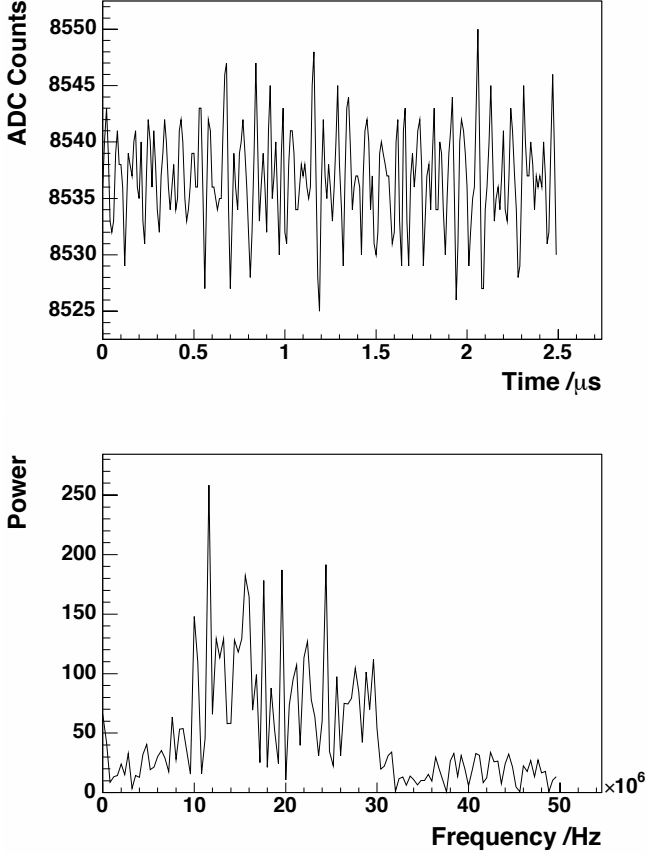


FIG. 39: Plots showing the noise at the digitiser without any signal (top) and the Fast Fourier Transform of that noise (bottom).

Introducing this value – along with the cavity parameters from the GdfidL simulation – into equation 63 and solving it against the shunt impedance resulted in a resolution for the BPM system of about 1 nm, assuming ideal electronics.

The additional noise introduced into the system by the electronics could be predicted using the specifications of the particular components and applying Friis’s formula for noise in a cascaded system [11]:

$$F = F_1 + \frac{F_2 - 1}{G_1} + \frac{F_3 - 1}{G_1 G_2} + \dots \quad (72)$$

where F was the total noise factor of the circuit, F_N was the noise factor of component N and G_N was the gain of component N (all dimensionless ratios). The theoretical signal diagram is shown in Figure 40. Using Friis’s formula, the theoretical gain of each separate signal channel was computed to be 39.0 dB with a noise figure of 3.1 dB.

The actual gain for each channel was measured by passing a known signal through the electronics and recording the output power (see Table III). The noise figures for each channel were measured by analyzing waveforms that

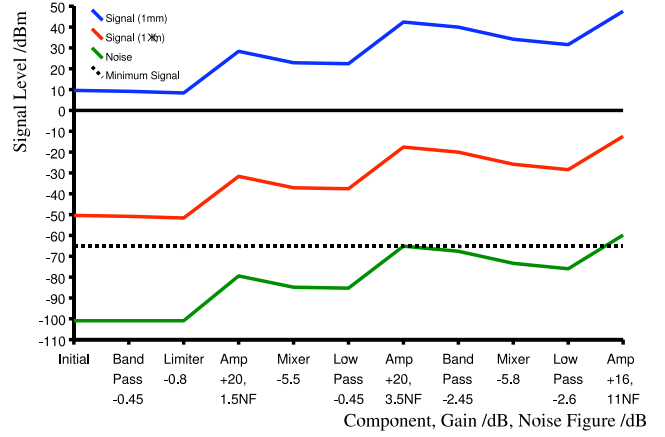


FIG. 40: Graph indicating the theoretical signal level at each component of the electronics.

Channel	Gain, dB	σ of ADC counts	Noise Figure, dB	Phase Noise, mrad
Reference	43.2	4.7	5.9	2.3
BPM 1, x	43.1	3.8	4.1	2.7
BPM 1, y	43.4	4.2	4.7	2.6
BPM 2, x	43.6	3.8	3.6	2.5
BPM 2, y	42.8	3.8	4.4	2.4
BPM 3, x	43.3	4.5	5.4	2.2
BPM 3, y	44.9	4.1	3.0	3.1

TABLE III: Table showing the measured gains, amplitude noise and noise figures for each BPM channel.

contained only thermal noise – no signal from a bunch transiting the cavity was present: The pedestal value was found by taking the mean of all 250 sample values, and the voltage noise was taken as the standard deviation. The voltage noise over 50 pulses (measured in ADC counts) was then averaged and converted to a power P using the formula

$$P = 10 \text{ dBm} \times \log_{10} \left(\frac{V^2/Z}{1 \text{ mW}} \right) \quad (73)$$

where V was the voltage measured at the ADCs and Z was the impedance (50Ω). By combining this with the measured gains and the theoretical level of thermal noise, the noise figures for each channel were found. These are listed in Table III.

2. Phase noise figure

Contributions to the phase noise came from both the local oscillators used down-convert the signal as well as from the digitizer. To quantify the level of this noise

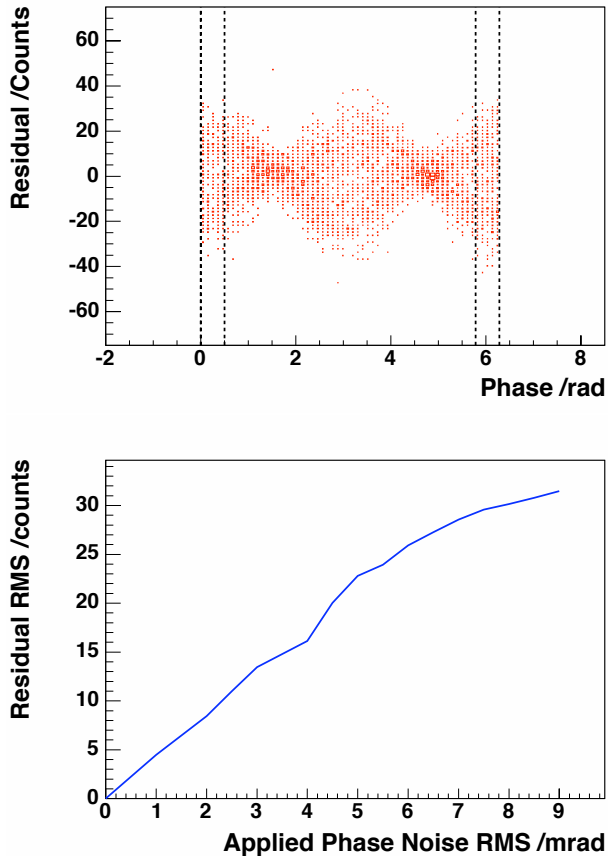


FIG. 41: Plot showing the variation of residual versus phase of the test tone.

present, a tone at the BPM frequency was applied to the electronics and the resultant waveforms recorded at the ADCs were fitted with a sine function

$$V = A \sin(\omega t + \varphi). \quad (74)$$

The residual between this fit and the data was plotted against phase ($\omega t + \varphi$) between 0 and 2π . A “bow-tie” effect, which can be seen in Figure 41, was interpreted as being due to phase noise in the system. At points where the slope of the sine wave was large ($\varphi = 0, \pi, 2\pi$), the residual was also large; at points where the slope of the sine wave was small ($\varphi = \pi/2, 3\pi/2$), the residual was small. This was as expected since the residual due to the phase noise was predicted to be proportional to the gradient of the waveform.

To estimate the phase noise present in each channel, simulated sine waves

$$V = A \sin(\omega t + \varphi). \quad (75)$$

were generated and added to the thermal noise data (i.e., no signal present from a bunch transiting the cavity) used in Section IX B 1. The amplitude of the generated

wave was set at the same value as that from the test-tone data. Phase noise was applied to these simulated pulses by adding a random gaussian component to the phase,

$$V = A \sin(\omega t + \varphi + \sigma_\varphi). \quad (76)$$

Performing the same sine wave fit to these generated pulses as was carried out on the data produced similar “bow-tie” style plots as seen in Figure 41, top plot. The magnitude of the bow-tie effect was found to be proportional to the phase noise applied, disappearing completely if the phase noise was removed altogether. To quantify the size of the bow-tie, the standard deviation of the residual for phase between $0 \rightarrow 0.5$ and $2\pi - 0.5 \rightarrow 2\pi$ was measured. By generating bow-tie plots for a range of values of phase noise, the correlation between phase noise and bow-tie size could be plotted, as shown in Figure 41, bottom plot. Using this relation, the size of the bow-tie in the data could be measured and the corresponding amount of phase noise found. This procedure was performed for all the channels and the amount of phase noise found in each is shown in Table III.

C. Predicting the Resolution

To predict the achievable resolution in a specific BPM channel with the level of noise as measured in Section IX B, the response of the fitting algorithm needed to be systematically analysed to determine the uncertainties in the fitted parameters. To accomplish this, simulated BPM responses to ATF extractions – modeled as exponentially decaying sine waves (see equation 7) – were generated for a range of amplitudes. The frequencies and decay constants as measured from data were used for the appropriate channel being simulated. The parameter t_0 was fixed. If a particular sample value was greater than the ADC maximum (16384 counts) or less than the ADC minimum (0 counts), the sample value was fixed at these limits, thus modeling the saturation seen in actual data. Phase and Thermal noise appropriate to each particular channel were also applied.

The simulated pulses were generated with amplitudes ranging between 0 and 25000 counts and then analysed using the fitting algorithm in the same way as the actual data. For each amplitude value, fifty simulated BPM signals were generated and analyzed, and the standard deviation of the fitted amplitude and phase were found. The dependence of these fitted values on the amplitude of the BPM signal is shown in Figures 42 and 43. A fourth order polynomial was used to fit to the amplitude curve in Figures 42 and an inverse dependence was used for the phase curve in Figure 43. Using these parameterizations, the uncertainty on the fitted amplitude and phase could be predicted given the amplitude of the waveform.

The position of the beam was calculated by normalizing both the amplitude and phase by the reference cavity and then performing an additional rotation given by the

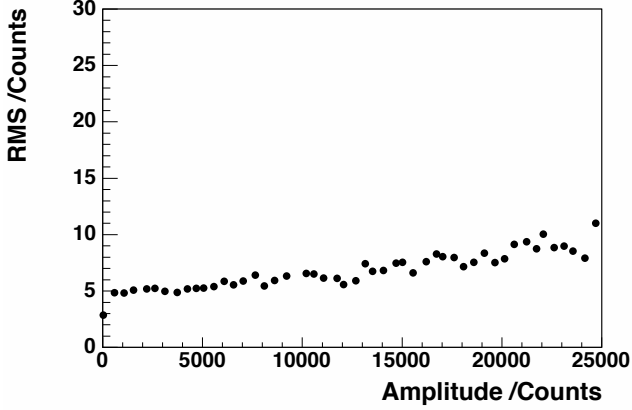


FIG. 42: Plot showing the variation with amplitude of the amplitude RMS.

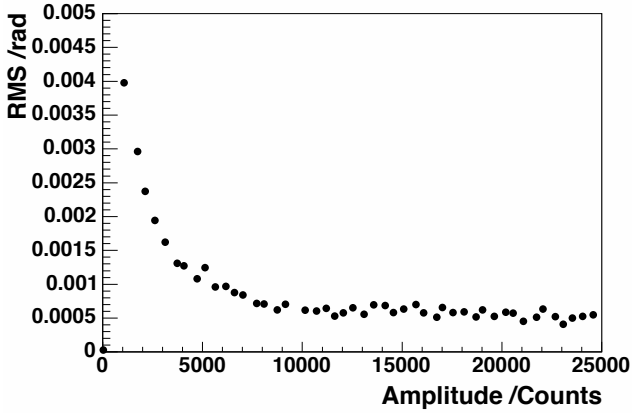


FIG. 43: Plot showing the variation with amplitude of the phase RMS.

IQ -phase, as ordinarily (described in Section IV, equations 8-11). This could be rewritten in the following form:

$$y_i = s_i \frac{A_i}{A_{\text{Ref}}} \cos(\varphi_i - \varphi_{\text{Ref}} - \Theta_i) \quad (77)$$

where y was the position, s the scale factor, A was the waveform amplitude, A_{Ref} was the reference amplitude, φ was the phase of the waveform, φ_{Ref} was the reference phase, and Θ was the rotation relating position and tilt to I and Q (see equation 10). Assuming the uncertainties were uncorrelated, the uncertainty on the position was given by:

$$\sigma_{y_i}^2 = \left(\sigma_{s_i} \frac{\partial y_i}{\partial s_i} \right)^2 + \left(\sigma_{A_i} \frac{\partial y_i}{\partial A_i} \right)^2 + \left(\sigma_{A_{\text{Ref}}} \frac{\partial y_i}{\partial A_{\text{Ref}}} \right)^2 + \left(\sigma_{\varphi_i} \frac{\partial y_i}{\partial \varphi_i} \right)^2 + \left(\sigma_{\varphi_{\text{Ref}}} \frac{\partial y_i}{\partial \varphi_{\text{Ref}}} \right)^2 + \left(\sigma_{\Theta_i} \frac{\partial y_i}{\partial \Theta_i} \right)^2 \quad (78)$$

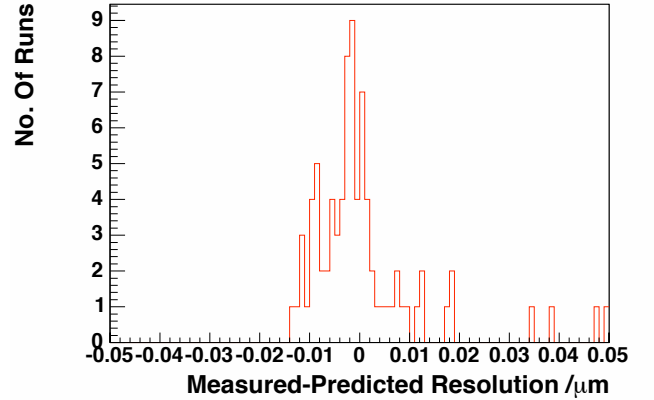
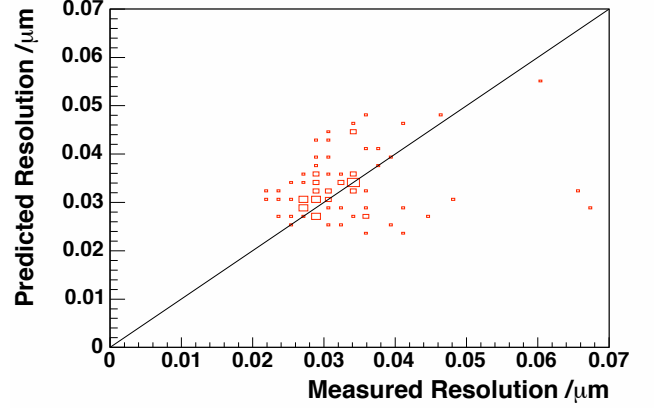


FIG. 44: Plots showing the predicted vs. measured resolutions (top) and the difference between the predicted resolution and the measured resolution (bottom).

The uncertainties associated with the determination of the IQ -phase Θ_i and scale factor s_i were assumed to be negligible, i.e. $\sigma_{s_i} = \sigma_{\Theta_i} \approx 0$.

The amplitude A_i and phase ($\varphi_i - \varphi_{\text{Ref}} - \Theta$) were computed by taking the mean of the set of BPM signals under study, and the resolution of a single BPM channel in isolation was computed using equation 78. The overall resolution was then calculated by summing in quadrature the resolutions for each individual channel, using the weights given by the result of the singular value decomposition (see Section VI, equation 38). This gave a prediction that could be directly compared to the measured resolution obtained using the method described in Section VI.

Using data taken on 27 May 2005 from a 2 hour run, the resolution was predicted for each set of 100 recorded ATF extractions. Each result was then compared with the measured resolution for the same 100 ATF extraction dataset. Significant correlation was found between the two (see Figure 44) indicating that the level of noise measured in Section IX B limits the achievable resolution of the BPMs.

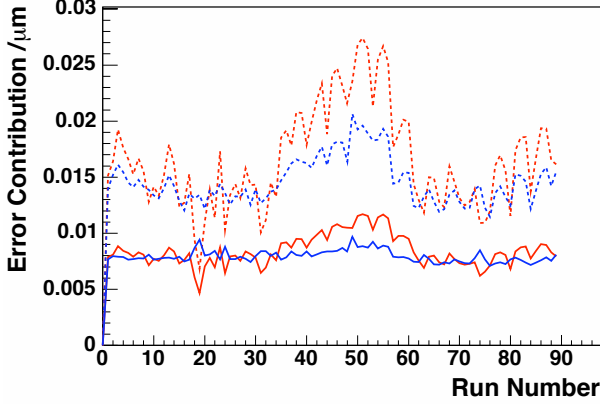


FIG. 45: Plots showing the relative contributions to the BPM resolution between the Amplitude (red) and Phase (blue) determination for the reference (dashed) and directional (solid) channels.

X. PROPOSED CHANGES TO IMPROVE RESOLUTION

Using the methods described in Section IX C, the dominant contributions to the resolution limit could be found and from this, possible ways to improve this limit. Initially, the resolution prediction (as given by equation 78) was broken down into four contributions, these being uncertainties in the determination of the amplitude and phase for both the reference cavity and the channel under study (y_2 was used throughout). The four contributions to the uncertainty are plotted in Figure 45, and show that the dominant contribution arises from the uncertainty in the determination of the reference cavity parameters. This was primarily as a result of the large weighting factor given by the y amplitude.

Additional information was provided by splitting up each contribution into the respective components due to phase and thermal noise, as shown in Figure 46. In the amplitude range of the y channel under study – typically between 10000 and 20000 ADC counts, neither source of noise was particularly dominant. However, for the amplitude range of the reference cavity – typically 3000 - 4000 counts, the thermal noise was dominant; particularly noteworthy was its contribution to the uncertainty in the waveform’s phase φ_{Ref} as shown in Figure 46, bottom plot.

After examination of this data, the following proposals are suggested to try to improve the resolution of the BPMs:

- Increasing the gain in the electronics associated with the reference cavity would improve its signal to noise ratio.
- Reducing the attenuation between the reference cavity and its electronics would also improve the

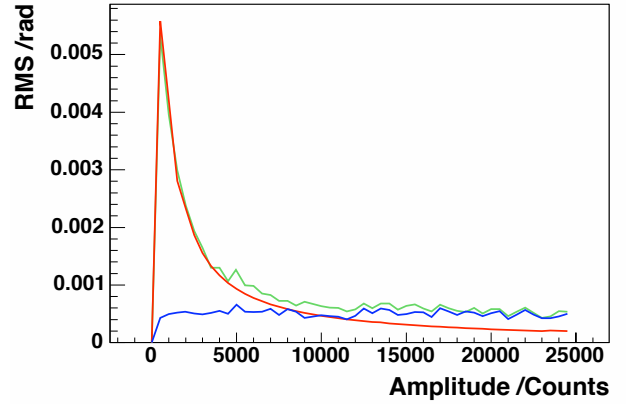
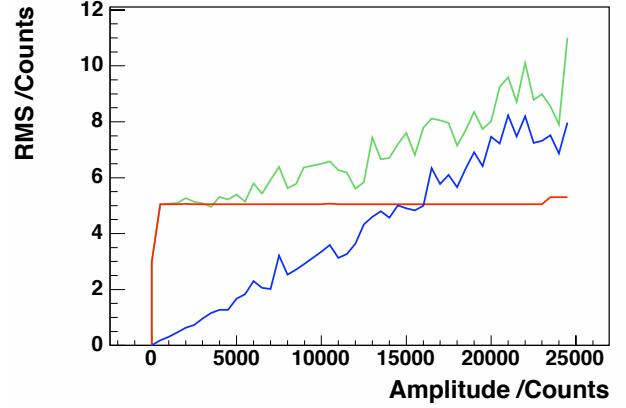


FIG. 46: Plots showing the contributions to the overall error in Amplitude determination (top) and Phase determination (bottom) from Thermal noise (red) and Phase Noise (blue) for the y_2 channel. Similar plots were found for the reference channel.

signal to noise ratio.

- Better centering the BPMs on the beam in all directions will reduce the effects of the reference cavity noise. Because the term $\partial y_i / \partial A_{\text{Ref}}$ in equation 78 is proportional to the y amplitude, reducing this weighting factor should improve the resolution. It should be possible to reduce the y amplitude to ~ 5000 counts giving an improvement in resolution of $\sim 30\%$.
- Increasing the bunch charge should increase the reference cavity amplitude and should decrease the error in the parameter determination for it. The minimum error possible from the reference cavity is at ~ 5000 counts. This should also improve the signal to noise in the directional cavities as well.
- Addressing the local oscillators used in the down-mix of the BPM signals may go some way in reducing the phase noise.

- Shortening the bunch length will increase the loss factor and improve the resolution.

XI. CONCLUSIONS

To date, we have demonstrated a resolution of less than 20 nm over short time periods spanning a minute or two, and a resolution of only slightly more than 20 nm over time periods spanning as long as half an hour. This resolution attains using two different analysis algorithms and is repeatable across multiple data sets.

Our plans for trying to improve on this resolution begin with improving the signal to noise in, most notably, the reference cavity, which may be accomplished by a combination of increasing the reference cavity gain and reduc-

ing the attenuation. Furthermore, better centering the directional BPMs on the beam will decrease the effects of this reference cavity noise on the resolution. Increasing the bunch charge will also have a positive effect on resolution by improving the signal to noise ratio in both the directional cavities as well as the reference cavity. Our resolution is also being limited by phase noise, and the local oscillators used in the down-mix of the BPM signals will have to be addressed. A higher loss factor (i.e. more power coupled out) would also go some length in improving the resolution, and one method for achieving this would be to shorten the bunches. The original 1 nm theoretical resolution prediction was based on the loss factor for a δ -function bunch, but the reality at ATF is a bunch which is approximately 1 cm long. There is clearly still room for improvement.

-
- [1] Draft letter of intent for the LINX test facility at SLAC. http://www-project.slac.stanford.edu/lc/linx/papers/LINX_07-15-01.pdf.
- [2] Tor Raubenheimer. Discussion of nanobeam summaries and areas for future collaboration. In *Web Proceedings of the 26th Advanced ICFA Beam Dynamics Workshop on Nanometre-Size Colliding Beams (Nanobeam 2002)*, Lausanne, Switzerland, 2002. ICFA. http://icfa-nanobeam.web.cern.ch/icfa-nanobeam/slides/raubenheimer_Nanobeams_summary_09-02.pdf.
- [3] Steve Smith. Private communication.
- [4] Zenghai Li, Stephen R. Smith, Takashi Naito, and Jeffrey Rifkin. Cavity BPM with dipole-mode selective coupler. In *Proceedings of the 2003 Particle Accelerator Conference*, Portland, OR, 2003. IEEE.
- [5] J. D. Jackson. *Classical Electrodynamics, Second Edition*. John Wiley and Sons, New York, 1975.
- [6] Milton Abramowitz and Irene A. Stegun. *Handbook of Mathematical Functions*. Dover Publications, Inc., New York, 1965.
- [7] V. Balakin et al. Discussion of nanobeam summaries and areas for future collaboration. <http://www.vlepp.serpukhov.su/engl/bnl/bpm.html>.
- [8] David J. Jackson, Dong Su, and Fred J. Wickens. Internal alignment of the SLD vertex detector using a matrix singular value decomposition technique. *Nucl. Instrum. Meth.*, A491:351–365, 2002. SLAC-PUB-9092.
- [9] Alexey Lyapin. *Strahllagemonitor fuer das TESLA-Energiespektrometer*. Dissertation, TU-Berlin, Berlin, 2003.
- [10] The GdfidL electromagnetic field simulator. <http://www.gdfidl.de>.
- [11] Devendra K. Misra. *Radio-Frequency and Microwave Communication Circuits, 2nd Ed.*, John Wiley and Sons, New York, 2004.
- [12] The latitude and longitude of the ATF were determined with a handheld GPS receiver. The earth's magnetic field and the rate of change of the field for that location for the date 11 March 2005 were then found on the website of the National Geophysical Data Center (NGDC) of the NOAA Satellite and Information Service: <http://www.ngdc.noaa.gov/seg/geomag/jsp/struts/calcPointIGRF>.